HHS Public Access

Author manuscript

Cell Rep. Author manuscript; available in PMC 2025 April 22.

Published in final edited form as:

Cell Rep. 2025 March 25; 44(3): 115374. doi:10.1016/j.celrep.2025.115374.

Astrocyte glypican 5 regulates synapse maturation and stabilization

Alexandra P. Bosworth[1,2], **Minerva Contreras**[1,2,5], **Laura Sancho**[1,5], **Isabel H. Salas**[1,5], **Adrien Paumier**[1], **Sammy Weiser Novak**[3], **Uri Manor**[3,4], **Nicola J. Allen**[1,6,*]

[1]Molecular Neurobiology Laboratory, The Salk Institute for Biological Studies, 10010 North Torrey Pines Rd., La Jolla, CA 92037, USA

[2]Neurosciences Graduate Program, University of California, San Diego, La Jolla, CA 92093, USA

[3]Waitt Advanced Biophotonics Center, The Salk Institute for Biological Studies, 10010 North Torrey Pines Rd., La Jolla, CA 92037, USA

[4]Department of Cell & Developmental Biology, University of California, San Diego, La Jolla, CA 92093, USA

[5]These authors contributed equally

[6]Lead contact

SUMMARY

The maturation and stabilization of appropriate synaptic connections is a vital step in neural circuit development; however, the molecular signals underlying these processes are not fully understood. We show that astrocytes, through production of glypican 5 (GPC5), are required for maturation and refinement of synapses in the mouse cortex during the critical period. In the absence of astrocyte GPC5, thalamocortical synapses show structural immaturity, including smaller presynaptic terminals, decreased postsynaptic density area, and presence of more postsynaptic partners at multisynaptic connections. This structural immaturity is accompanied by a delay in developmental incorporation of GLUA2-containing AMPARs at intracortical synapses. The functional impact of this is that mice lacking astrocyte GPC5 exhibit increased levels of ocular dominance plasticity in adulthood. This demonstrates that astrocyte GPC5 is necessary for maturation and stabilization of synaptic connections, which has implications for disorders with altered synaptic function where GPC5 levels are altered, including Alzheimer's disease and frontotemporal dementia.

*Correspondence: nallen@salk.edu.

AUTHOR CONTRIBUTIONS

A.P.B., M.C., S.W.N., L.S., I.H.S., A.P., and N.J.A. performed experiments and analyzed data. U.M. and N.J.A supervised experiments. A.P.B. and N.J.A. designed the experiments and wrote the paper with input from all authors. N.J.A. conceived the project.

DECLARATION OF INTERESTS

The authors declare no competing interests.

SUPPLEMENTAL INFORMATION

Supplemental information can be found online at https://doi.org/10.1016/j.celrep.2025.115374.

In brief

Bosworth et al. demonstrate that astrocyte-expressed glypican 5 regulates glutamatergic synapse maturation and stabilization in the developing cortex, identifying a role for this factor in astrocytes in sculpting developing neural circuits.

Graphical Abstract

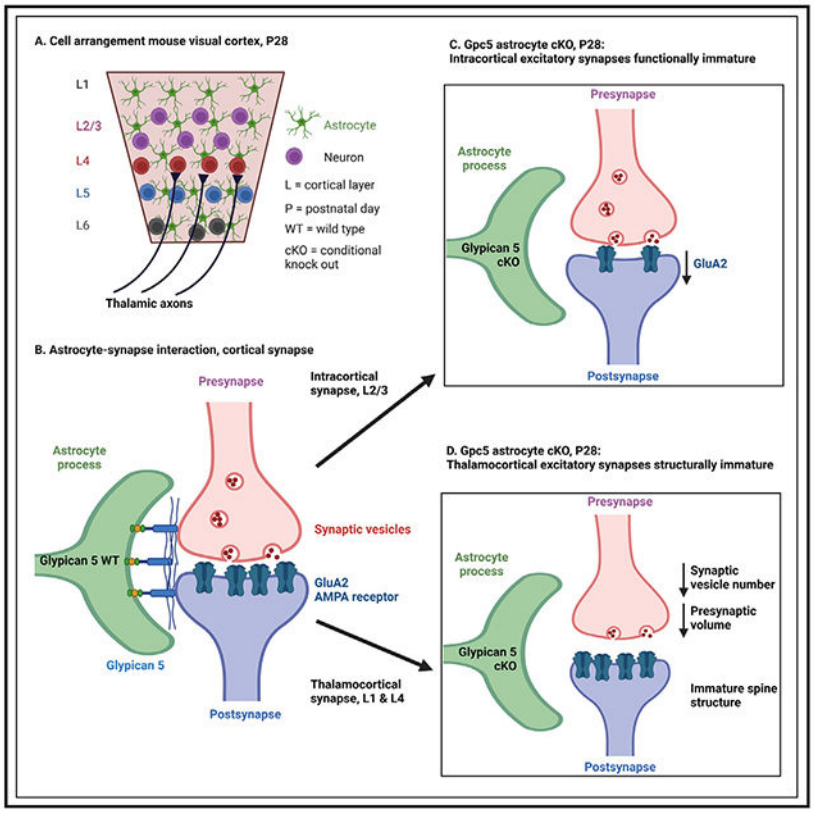

INTRODUCTION

The formation and maturation of neuronal synapses during development is essential for circuit function throughout the life span. The transformation from immature nascent synapses to stable mature synapses in the adult involves structural changes at the pre- and postsynaptic terminals as well as shifts in neurotransmitter receptor composition. In the cortex, functional maturation of excitatory glutamatergic synapses is marked by the incorporation of GLUA2 subunits into α-amino-3-hydroxy-5-methyl-4-isoxazolepropionic acid (AMPA)-type glutamate receptors (AMPARs) which renders them impermeable to calcium.[1,2] Structurally, immature filopodium-like dendritic spines mature into a more stable mushroom-like structure as the synapse is strengthened and stabilized.[3] These processes result in more stable synaptic connections that make up the persistent cortical circuits observed in the adult. The mechanisms that drive this developmental switch in synaptic structure and receptor composition and that maintain stable connections in the adult brain are not fully understood.

Astrocytes, a class of glial cells, produce several secreted proteins that regulate the formation and maturation of synapses.[4,5] Thrombospondin 1 and 2 induce structurally immature excitatory synapses to form, and Hevin regulates postsynaptic spine maturation.[6,7] Glypican 4 and 6 induce the formation of nascent glutamatergic synapses by increasing levels of GLUA1 AMPARs, and chordin-like 1 (CHRDL1) contributes to synapse maturation by recruitment of GLUA2 AMPARs.[8–10] Glypicans (GPCs) are Glycosylphosphatidylinositol (GPI)-anchored heparan sulfate proteoglycans, and there are 6 family members in mammals (GPC1–GPC6).[11] GPCs exist in a membrane-attached form or are cleaved from the membrane to produce a soluble form, which has been shown to be synaptogenic when produced by astrocytes.[8] GPCs are expressed in the brain at different stages of development and adulthood by multiple cell types and have roles in regulating synapses.[12–14] Given the synaptogenic role of astrocyte GPC4 and GPC6 in early development, we asked whether other GPC family members are expressed by astrocytes and, if so, whether they play a role in regulating synapses. This led us to focus on GPC5, which is expressed widely across the brain and whose expression by astrocytes is increased during a time of robust synaptic maturation and refinement in the cortex and remains highly expressed in the adult brain.[15]

The timing of GPC5 expression suggests that it may regulate synapse maturation and maintenance in the adult, which we addressed in the mouse visual cortex (VC). Within the primary VC, excitatory presynaptic inputs come from two main sources: intracortical and thalamocortical axons. Intracortical inputs can be distinguished by expression of VGLUT1 at their presynaptic terminals, while thalamocortical inputs, arising from the visual thalamus (dorsal lateral geniculate nucleus (dLGN)), express VGLUT2 at their presynaptic terminals.[16,17] Thalamic inputs make up a small fraction of the excitatory connections in the VC but are distinct due to the large size of the axonal boutons and the presence of multiple postsynaptic targets at a single bouton.[18–20] Both intracortical and thalamocortical synapses undergo a developmental incorporation of GLUA2 AMPAR subunits as they mature, which occurs in a layer-dependent manner between post-natal day 7 (P7) and P16.[1,2] Normal development of the VC involves the refinement of thalamocortical synapses as ocular dominance is established and neurons in the binocular zone (BZ) are tuned for binocular matching of the eyes, which continues during the critical period, a time of enhanced plasticity.[21,22]

Using astrocyte-specific *Gpc5* conditional knockout (cKO) mice, we found that the absence of astrocyte GPC5 renders thalamocortical synapses structurally immature and delays the incorporation of GLUA2 at intracortical synapses during the critical period, demonstrating that GPC5 regulates synapse maturation. Further, in mice lacking astrocyte GPC5, we found an increase in plasticity in response to visual deprivation in adulthood, showing that GPC5 is a plasticity-restricting factor in the adult. The role of GPC5 as a regulator of synapse maturation and plasticity is distinct from the roles of GPC4 and GPC6 in synapse formation, showing diverse roles for different GPC family members in cortical circuit development and maturation.

RESULTS

Gpc5 is expressed throughout the brain by both astrocytes and OPCs

To determine when *Gpc5* is expressed in the developing brain, we consulted our published RNA sequencing dataset of mouse VC astrocytes across distinct stages of synaptic development: P7, synapse initiation; P14, synaptogenesis peaks; P28, synapse maturation (peak critical period); P120, synapses stable (adulthood) (Figure 1A).[15] This showed that astrocyte *Gpc5* mRNA is upregulated between P7 and P14 and remains highly expressed throughout adulthood (P28 and P120) (Figure 1B). In contrast, other astrocyte-expressed GPC family members, *Gpc4* and *Gpc6*, peak in expression at P7 and P14, respectively, and then decline (Figure 1B). Additionally, the level of *Gpc5* mRNA in astrocytes is ~10-fold higher than either *Gpc4* or *Gpc6* at the peak of expression (Figure 1B), demonstrating that *Gpc5* is the predominant GPC in astrocytes. To determine whether additional cell types express *Gpc5*, we consulted published RNA sequencing studies, which show that *Gpc5* mRNA is enriched in both astrocytes and oligodendrocyte progenitor cells (OPCs) compared to other cells, including neurons and microglia (Figure 1C).[23] Thus, *Gpc5* is enriched in the glial lineage.

To ask how broadly expressed *Gpc5* is across the mouse brain, we consulted published RNA sequencing studies. These show that *Gpc5* is highly expressed by adult astrocytes in the forebrain, particularly the cortex, and at a lower level in cerebellar astrocytes (Figure S1A).[24,25] To validate this, we performed spatial analysis of *Gpc5* mRNA using single-molecule fluorescent *in situ* hybridization (smFISH) in sagittal sections of the P28 mouse brain, showing widespread signal across brain regions (Figure 1D). Due to the higher expression of *Gpc5* by cortical astrocytes (Figure S1A) and our time-course analysis of *Gpc5* expression in VC astrocytes, we focused on the VC for further studies. smFISH of *Gpc5* showed homogeneous expression across all layers of the VC at P28 (Figure 1F).[15] Based on the temporal expression of *Gpc5*—upregulated at P14 and remaining high into adulthood—and the known role of other GPC family members in regulating synaptic development, we hypothesized that GPC5 plays a role in regulating synaptic maturation and/or stability.

To test this hypothesis, we developed an astrocyte-specific *Gpc5* knockout mouse by crossing mice with a floxed allele of *Gpc5* to mice expressing cre recombinase in astrocytes (*Gfap-cre 73.12*), and compared $Gpc5^{fl/fl}$ cre-negative (wild-type [WT]) and $Gpc5^{fl/fl}$ cre-positive (cKO) littermates (Figure 1E). To verify astrocyte-specific removal of GPC5, we performed smFISH for *Gpc5* in P28 cKO and WT VCs along with an astrocyte (*Slc1a3*) and an OPC probe (*Cspg4*) (Figure 1G). In WT mice, we detected widespread expression of *Gpc5* throughout the VC in both astrocytes and OPCs (Figures 1G and S1B). In *Gpc5* cKO mice, *Gpc5* expression was significantly decreased in astrocytes but not OPCs, demonstrating specificity of the knockdown (Figures 1H, 1I, and S1C). *Gpc5* cKO mice retained some *Gpc5* expression in the cortex due to OPC expression (Figure S1D). To further validate the model, we performed smFISH for *Gpc5* in P28 cKO and WT VCs along with immunostaining for the astrocyte marker protein S100beta and a neuronal probe (*Tubb3*) (Figure S1E). In this analysis, *Gpc5* expression is significantly decreased in

astrocytes, but not neurons, in *Gpc5* cKO mice, further demonstrating knockdown specificity (Figures S1F and S1G). We detected no difference in the size of astrocytes marked by the different methods (*Slc1a3* and S100beta), suggesting that no gross change in astrocyte morphology occurs in the *Gpc5* cKO condition (Figures S1H and S1I). Additionally, we asked whether there is a compensatory response in astrocytes to knocking out GPC5 by probing for two other astrocyte-expressed GPCs, *Gpc4* and *Gpc6*, and the synaptogenic protein *Chrdl1* and found no significant differences (Figures S1J–S1N). This shows that *Gpc5* is enriched in glial cells in the mouse VC and that removing GPC5 from astrocytes does not cause a compensatory upregulation of *Gpc5* in OPCs or neurons or of *Gpc4, Gpc6*, or *Chrdl1* in astrocytes.

Synapses in *Gpc5* cKO mice are immature during the critical period

Due to the role of other GPC family members expressed by astrocytes, GPC4 and GPC6, in regulating synaptic development and levels of GLUA1 containing AMPARs, we first asked whether GPC5 regulates the number of synapses or their AMPAR composition. Due to the uniform expression of *Gpc5* across upper and lower layers of the VC and the maintained high expression of *Gpc5* at P28, the peak of the critical period, we analyzed both thalamocortical and intracortical synapses within the VC at this time point. To determine the number and AMPAR composition of synapses, we used immunohistochemistry to label presynaptic markers VGLUT1 (for intracortical synapses) and VGLUT2 (for thalamocortical synapses) and postsynaptic markers GLUA1 (immature synapses) and GLUA2 (mature synapses), visualized using confocal microscopy (Figures 1E, 2, and S2).

To determine intracortical synapse numbers and AMPAR composition, we analyzed colocalization of GLUA1 or GLUA2 with the presynaptic marker VGLUT1 in layer 1 (L1) and L2/3 of WT and *Gpc5* cKO mice. This showed a significant, ~30% decrease in the colocalization of GLUA2 and VGLUT1 in L2/3 with no difference in L1 (Figures 2A–2D, S2A, and S2D). This is driven by a decrease in GLUA2 puncta in L2/3 with no difference in L1 and no alteration in the number of presynaptic terminals marked by VGLUT1 (Figures 2A–2C and S2A–S2C). In the case of GLUA1, we found no difference in the number of GLUA1 puncta in L1 or L2/3 or in the colocalization of GLUA1 and VGLUT1 in either layer (Figures 2E–2H and S2E–S2H). This shows that, in the absence of astrocytic GPC5, intracortical synapses lack GLUA2 specifically in L2/3.

To investigate whether there are alterations at thalamocortical synapses in *Gpc5* cKO mice, we quantified the colocalization of the presynaptic marker VGLUT2 with postsynaptic GLUA1 or GLUA2 in L1 and L4, where thalamocortical synapses predominantly form. We found no significant difference in the colocalization between VGLUT2 and GLUA1 in either L1 or L4 or in the number of GLUA1 or VGLUT2 puncta (Figures 2M–2P and S2M–S2P). There was no difference in colocalization of VGLUT2 and GLUA2 in L1 or L4 or in the number of GLUA2 or VGLUT2 puncta (Figures 2I–2L and S2I–S2L). While the number of presynaptic VGLUT2 terminals is not altered between WT and *Gpc5* cKO mice, we found a significant, ~40% decrease in the volume of VGLUT2 puncta in both L1 and L4 (Figures 2Q–2S).

These data show that intracortical and thalamocortical synapses have distinct developmental aberrations in the VC of *Gpc5* cKO mice during the critical period (Figure 2T), with decreased GLUA2 at intracortical synapses and apparently smaller presynaptic terminals at thalamocortical synapses. Together, this suggests that astrocyte GPC5 contributes to synapse maturation in the developing VC.

Intracortical synapses in *Gpc5* cKO mice show reduced functionality during the critical period

Given the decreased level of GLUA2 AMPARs present at intracortical synapses in L2/3 during the critical period (Figures 2A–2D), we next asked whether this has any impact on synaptic function of neurons in this layer. We performed *ex vivo* whole-cell patch-clamp recordings from L2/3 pyramidal neurons in acute slices of VC from *Gpc5* cKO and WT mice at P28.[10] We recorded AMPA-mediated spontaneous excitatory postsynaptic currents (sEPSCs) by pharmacologically blocking N-methyl-D-aspartate (NMDA) and γ-aminobutyric acid (GABA) A receptors. This demonstrated that, in the absence of astrocytic GPC5, sEPSCs are significantly reduced in amplitude, with no impact on the frequency or kinetics of events detected (Figures 3A–3E). This suggests that the reduced level of GLUA2 AMPARs detected using immunohistochemistry results in decreased strength of this synaptic connection.

Thalamocortical synapses are structurally immature in *Gpc5* cKO mice during the critical period

The decrease in VGLUT2 puncta volume observed by confocal microscopy in *Gpc5* cKO mice suggests a presynaptic structural deficit at thalamocortical synapses (Figures 2Q–2S). This could be due to decreased size of the presynaptic axonal bouton and/or decreased numbers of presynaptic vesicles containing VGLUT2. We investigated this at the ultrastructural level using electron microscopy (EM). To specifically analyze thalamocortical synapses formed between neurons originating in the visual thalamus (dLGN) and L4 target neurons in the VC, we labeled mitochondria within these axons using the EM marker APEX2.[26] We injected AAV2/9-COX4-dAPEX2 into the dLGN of WT and *Gpc5* cKO mice at P14 and collected brains at P28, performing processing for EM and treatment with diaminobenzidine (DAB) to visualize APEX2-labeled mitochondria (Figure 4A). Serial sections were collected and imaged in the scanning electron microscope, and high-resolution volumes of neuropil (3 dimensional EM) were assembled.

Within the VC, the APEX2-DAB labeled mitochondria of the dLGN projections were identifiable in L4, where these projections synapse. For analysis, thalamocortical presynaptic boutons were identified by the presence of DAB-labeled mitochondria within the parent axon, and thalamic connections were traced and reconstructed (Figure 4B; Video S1). Labeled boutons had the features of VGLUT2-positive thalamic synapses, including a large volume, asymmetric synapses, and multiple postsynaptic contacts at some presynaptic sites. In each analysis, we compared features of WT and *Gpc5* cKO synapses as a single group, as well as analyzed monosynaptic and multisynaptic connections as separate groups.

We found that the average volume of presynaptic boutons in *Gpc5* cKO mice is significantly decreased compared to the WT (Figure S3A). This result is driven by a significant decrease in the volume of multisynaptic boutons in *Gpc5* cKO mice, with no difference in the volume of monosynaptic boutons (Figures 4C and 4D). In both genotypes, there is a significant increase in the volume of multisynaptic boutons compared to monosynaptic boutons, as expected, but this increase is smaller in *Gpc5* cKO mice (Figure 4D). The number of synaptic vesicles within multisynaptic boutons is significantly decreased in *Gpc5* cKO mice compared to the WT, with no change at monosynaptic connections (Figures 4C–4E and S3B). Additionally, we found that the average number of postsynaptic partners at a multisynaptic bouton is higher in *Gpc5* cKO mice compared to the WT, and that the maximum observed number of synapses at a single bouton is also greater in *Gpc5* cKO mice (Figures 4F and 4G).

These results demonstrate that there are structural alterations at thalamocortical synapses in *Gpc5* cKO mice that are particularly pronounced at multisynaptic connections. The decreased VGLUT2 puncta volume observed by light microscopy (Figures 2Q–2S) is likely a result of the decreased volume of *Gpc5* cKO multisynaptic thalamic boutons and decreased total number of vesicles per bouton. These alterations, as well as the larger number of postsynaptic contacts at multisynaptic boutons, suggests that the absence of astrocytic GPC5 renders thalamocortical synapses more immature.[3,27,28]

Gpc5 cKO mice show altered postsynaptic structure at thalamocortical synapses during the critical period

Our data demonstrate that there are developmental disruptions in the presynaptic structure of thalamocortical synapses, and the synaptic AMPAR composition of intracortical synapses, in the absence of GPC5 (Figures 2, 3, and 4). We next asked whether these effects are accompanied by a change in postsynaptic structure of either thalamocortical or intracortical synapses.

To specifically analyze the postsynaptic ultrastructure of thalamocortical synapses, we used the EM dataset and segmented the postsynaptic partners of the reconstructed APEX2-labeled presynaptic boutons. The predominant postsynaptic structures identified were dendritic spines, with labeled synapses directly on the dendritic shaft rarely observed. To characterize the postsynaptic compartment, we measured the surface area of the postsynaptic density (PSD), finding a significant decrease in PSD surface area in *Gpc5* cKO mice (Figures 5A, 5B, and S4A). This decrease is present at spines opposed to both monosynaptic and multisynaptic boutons (Figure 5B). We asked whether postsynaptic spine structure is impacted and classified reconstructed spines as thin, mushroom, or other based on morphology. When analyzing all connections together, we found no significant differences (Figure S4B), with an increased percentage of thin spines and a decreased percentage of mushroom spines detected in the *Gpc5* cKO when separated into those present at monosynaptic or multisynaptic connections (Figure S4C). To ask which connection type is responsible for this difference, we analyzed them separately, finding a significant increase in the percentage of thin spines and decrease in mushroom spines at monosynaptic connections

(Figure 5C), with no significant shift at multisynaptic connections in *Gpc5* cKO mice (Figure 5D).

Given the decreased GLUA2 levels at L2/3 intracortical synapses in the P28 *Gpc5* cKO mice, we next asked whether there was a shift toward a more immature dendritic spine structure in neurons in this layer, which consists of predominantly intracortical synapses. We used sharp electrodes to fill individual L2/3 pyramidal neurons in the VC with fluorescent dye in acute brain sections of P28 WT and *Gpc5* cKO mice, with spines imaged using confocal microscopy (Figure 5E). We found no significant difference in the average spine density on apical or basal dendrites of L2/3 neurons (Figures 5F and 5G). Analysis of spine morphology (width, length, and length to width ratio) also showed no difference between genotypes (Figures S4D–S4I). We further categorized spines as mushroom, thin, or stubby based on these measurements, finding no differences in categorization between the genotypes for either apical or basal dendrites (Figures 5H and 5I). Overall, we did not observe any gross changes in the structure of spines on dendrites of L2/3 neurons in *Gpc5* cKO mice.

The decreased PSD surface area at thalamocortical synapses in *Gpc5* cKO mice indicates that the strength of thalamocortical synapses is diminished, while the shift toward an increased prevalence of immature thin spines suggests that thalamocortical synapses are more immature. This immature postsynaptic phenotype, and the smaller and less refined thalamic axonal boutons described above, indicate that the absence of astrocytic GPC5 disrupted the maturation of thalamocortical synapses.

GPC5 is sufficient to regulate synaptic receptor composition

Analysis of synapses in the VC of *Gpc5* cKO mice showed a number of alterations, including structurally immature thalamocortical synapses and decreased GLUA2 at intracortical synapses. To gain insight into the site of action of GPC5 (i.e., presynaptic or postsynaptic), we performed two sets of experiments. First, we used retinal ganglion cell (RGC) neurons in culture to determine whether soluble GPC5 is sufficient to induce synapses to form. We used RGCs because they form few synapses in the absence of astrocytes and have been used to study the role of astrocyte-secreted proteins in synaptogenesis, including GPC4 and CHRDL1.[4,10] Second, we asked whether local delivery of GPC5 to the VC of *Gpc5* cKO mice would be sufficient to regulate presynaptic features, postsynaptic features, or both.

RGCs were cultured alone, with astrocytes, or with recombinant GPC5 protein added to the medium for 6 days and then immunostained for presynaptic VGLUT2 and postsynaptic PSD95 (Figure S5A). Analysis of colocalized VGLUT2 and PSD95, to mark synapses, showed a significant increase in synapse number in RGCs cultured with astrocytes compared to alone, with no effect of soluble GPC5 (Figure S5B), demonstrating that GPC5 is not sufficient to induce synapse formation by itself. Due to altered presynaptic terminals identified in *Gpc5* cKO mice, we analyzed whether soluble GPC5 protein was sufficient to impact VGLUT2 presynaptic specializations. This identified that GPC5 significantly increased the number of presynaptic sites compared to RGCs cultured alone, though this increase was less than that induced by astrocytes (Figure S5C). Analysis of the size of

presynaptic terminals found no significant increase after treatment with GPC5, whereas astrocytes did induce larger terminals (Figures S5D and S5E). This suggests that a site of action of soluble GPC5 is presynaptic, the same as for other astrocyte-expressed GPCs, including GPC4.[9]

To assess the ability of GPC5 to regulate synapses *in vivo*, we used a viral strategy to overexpress hemagglutinin (HA)-tagged GPC5, or the control protein membrane-GFP, in astrocytes of *Gpc5* cKO mice. We used local injection of AAV2/5 into the VC, driving expression of cargo under the minimal Gfap promoter to target astrocytes, with delivery at P14 and analysis at P28 (Figures 6A and 6B). Costaining for the HA tag and the astrocyte marker protein S100beta demonstrated high specificity and efficiency of transduction (Figures S6A–S6C), while immunostaining for GPC5 validated the production of GPC5 protein (Figure S6D). We used immunostaining to assess features of synapses that are impacted in *Gpc5* cKO mice (Figure 2). VC L2/3 intracortical synapses in *Gpc5* cKO mice have less GLUA2 and less VGLUT1-GLUA2 colocalization with no difference in VGLUT1. We observed that overexpression of GPC5 is sufficient to increase total level of GLUA2 (Figures 6C and 6D) without impacting VGLUT1 or colocalization (Figures S6G and S6H). VC L4 thalamocortical synapses have a decreased volume in *Gpc5* cKO mice (Figure 2S); overexpression of GPC5 did not impact VGLUT2 terminal volume (Figures S6E and S6F), the same as observed in RGCs in culture (Figure S5).

These data show that addition of GPC5 is sufficient to increase the number but not size of presynaptic VGLUT2 sites *in vitro* in RGCs, and increase the level of GLUA2 at intracortical synapses in *Gpc5* cKO mice *in vivo*. In contrast, GPC5 delivery did not impact VGLUT2 terminal volume *in vitro* or *in vivo*. These results suggest an ability of GPC5 to directly increase postsynaptic GLUA2 at intracortical connections independent of an effect on thalamocortical synapses. Second, at this time point, GPC5 cannot rescue the thalamocortical presynaptic deficit, either because this requires an earlier intervention or, alternatively, because this deficit is secondary to a dendritic phenotype of these neurons in the thalamus.

Large-scale ocular dominance plasticity during the critical period is unchanged in *Gpc5* cKO mice

Gpc5 cKO mice show features of immature synapses at P28, the peak of the critical period, leading us to ask whether *Gpc5* cKO mice show enhanced experience-dependent plasticity at this time point, when plasticity is already high and brief periods of sensory deprivation are sufficient to alter neuronal connectivity. In the BZ of the VC, this plasticity can be observed by depriving one eye of vision for a number of days, which induces neurons from the open eye to expand their territory in the BZ.

Gpc5 cKO and WT mice were monocularly enucleated (ME) at P28, and the extent of BZ remodeling was assessed after 12 hours (baseline innervation) or 5 days (remodeling) by exposing mice to bright light to activate neurons in the VC and induce expression of the immediate-early gene *Arc*, visualized using smFISH (Figure 6E).[29] The width of the *Arc* signal represents the BZ innervated by the intact eye, and expansion of the *Arc* signal following ME provides a measurement of ocular dominance plasticity. After 12 hours of

deprivation, we found no difference in the width of the *Arc*-activated neuron zone between *Gpc5* cKO mice and the WT, indicating that absence of astrocyte GPC5 does not alter baseline connectivity (Figures 6F and 6G). In both the WT and *Gpc5* cKO mice, 5 days of ME are sufficient to significantly increase the width of the *Arc* signal compared to 12 hours, indicating that remodeling has occurred. Furthermore, we found no significant difference between WT and *Gpc5* cKO mice in the width of the *Arc* signal following 5 days of deprivation (Figures 6F and 6G), demonstrating that lack of GPC5 in astrocytes does not affect large-scale sensory remodeling during the critical period.

Synapse maturation is delayed in *Gpc5* cKO mice

As *Gpc5* remains highly expressed in the adult brain, we asked whether adult mice lacking GPC5 maintain deficits in synaptic AMPAR composition and presynaptic terminal size (Figure 2). We assessed this using immunohistochemistry and confocal imaging of synapses in the VC of *Gpc5* cKO and WT mice at P120. We analyzed intracortical and thalamocortical synapses using the presynaptic markers VGLUT1 and VGLUT2 respectively, and focused on the AMPAR subunit GLUA2 due to the decreased level we observed at P28.

At intracortical synapses, we found no significant difference in VGLUT1 or GLUA2 puncta numbers or colocalization of VGLUT1 and GLUA2 between WT and *Gpc5* cKO mice in either L1 or L2/3 (Figures 7A–7H). This is in contrast to P28, where total GLUA2 and VGLUT1-GLUA2 synapses are decreased in L2/3 in *Gpc5* cKO mice (Figure 2). At thalamocortical synapses, we found no difference in VGLUT2 or GLUA2 puncta numbers or colocalization of VGLUT2 and GLUA2 between WT and *Gpc5* cKO mice in either L1 or L4 (Figures S7A–S7H). This is consistent with findings at P28 (Figure 2). We found no difference in the volume of VGLUT2 puncta between WT and *Gpc5* cKO mice in either L1 or L4 (Figures 7I–7K), in contrast to P28, where terminal volume is decreased in *Gpc5* cKO mice (Figure 2). Taken together, these data indicate that, by P120, synaptic alterations detected during the critical period in *Gpc5* cKO mice have been rectified (Figure 7L), suggesting that absence of astrocytic GPC5 delays rather than prevents synapse maturation.

Absence of astrocyte GPC5 enables enhanced ocular dominance plasticity in adulthood

In adulthood, the high level of experience-dependent plasticity present during the critical period is decreased, and brief periods of sensory deprivation are insufficient to induce large-scale remodeling. Although steady-state synapse numbers and AMPAR composition in *Gpc5* cKO mice have reached WT levels in adulthood (Figures 7 and S7), the continued high expression of GPC5 by astrocytes in the adult brain (Figure 1B) led us to ask whether absence of GPC5 enables increased ocular dominance plasticity in *Gpc5* cKO mice in adulthood.

We performed ME in *Gpc5* cKO and WT mice at P120 and probed for changes in VC neural connectivity using smFISH for *Arc* to visualize active neurons, as described at P28 (Figure 6E). We found no difference in the width of the *Arc* zone between WT and *Gpc5* cKO mice after 12 hours of ME, indicating that no baseline changes in connectivity are present at P120 (Figures 7M and 7N). After 5 days of ME, we found no difference in the width of

the *Arc* zone in WT mice when compared to 12 hours deprivation, consistent with limited plasticity present in the adult brain (Figures 7M and 7N). For *Gpc5* cKO mice, we found a significant increase in the width of the *Arc* zone after 5 days of ME compared to 12 hours, demonstrating that absence of astrocytic GPC5 has enabled some plasticity to occur (Figures 7M and 7N). The width of the *Arc* zone after 5 days of ME is also significantly larger in *Gpc5* cKO mice compared to the WT (Figures 7M and 7N). This demonstrates that lifelong absence of GPC5 specifically in astrocytes enables an environment that is permissive to plasticity and neuronal remodeling in the adult brain (Figure 7O).

DISCUSSION

This study identified that astrocyte GPC5 regulates excitatory synapse maturation and stabilization. In the absence of astrocytic GPC5, the structural maturation and refinement of thalamocortical synapses is impaired, and the level of GLUA2 AMPARs at intracortical synapses is reduced. The consequence of this is enhanced remodeling of connections in the VC after visual deprivation in the adult brain but not during the critical period, suggesting that, in the adult brain, GPC5 represses plasticity. Importantly, these effects are observed in the presence of continued GPC5 expression in OPCs, suggesting that there may be distinct roles for GPC5 depending on the cell type of origin. These actions are also distinct from those of other astrocyte-expressed GPC family members. GPC4 and GPC6 induce nascent synapse formation via clustering of GLUA1 AMPARs, distinct from GPC5, which regulates synapse maturation and GLUA2 AMPARs with no impact on GLUA1.[8,9] Other astrocytic factors that regulate synapse maturation also have distinct actions from GPC5. CHRDL1 recruits GLUA2 AMPARs predominantly to thalamocortical synapses, whereas the effect of GPC5 on GLUA2 is restricted to intracortical synapses.[10] Further, *Chrdl1* KO mice show enhanced ocular dominance plasticity during the critical period and in adulthood, whereas the impact of astrocyte GPC5 on large-scale plasticity is limited to adulthood. In addition, Hevin regulates NMDA receptors and spine maturation without impact on AMPA receptors.[6] This shows that, while astrocytes produce multiple synapse-regulating factors, each has a distinct action in regulating the development and maturation of excitatory synapses.

We found that astrocyte GPC5 regulates thalamocortical synapse maturation, with these connections showing smaller bouton size, fewer synaptic vesicles, and a smaller PSD surface area in *Gpc5* cKO mice.[28,30,31] The presence of weaker synapses in conjunction with a greater number of postsynaptic partners at multisynaptic boutons suggests that this circuit is not undergoing typical maturation, whereby selected synapses are strengthened and stabilized and excess synapses are pruned.[3,18] We hypothesize that GPC5 is necessary for the strengthening of appropriate synapses and that, in the absence of this strengthening, pruning may be disrupted, leading to excessive weaker synaptic connectivity. Weaker synapses with more immature dendritic spine morphologies are indicative of a less stable synaptic connection, and in the adult, destabilized axonal boutons have been associated with cognitive decline.[32] Furthermore, GPC5 positively regulates the level of GLUA2 at intracortical synapses, and GLUA2 is associated with mature, stable synapses. Diminished GPC5 expression may therefore contribute to synapse loss via destabilization of connections, which is of interest, as decreased GPC5 expression has been associated

with multiple neurological disorders that show synaptic dysfunction, including Alzheimer's disease, frontotemporal dementia, and schizophrenia.[33–36]

In the absence of GPC5 in astrocytes, brief visual deprivation in adulthood is sufficient to induce plasticity, whereas absence of GPC5 does not enhance the level of plasticity that normally occurs during the critical period. This suggests that GPC5 may be involved in actively repressing plasticity after the closure of the critical period. The astrocyte-secreted factor CHRDL1 represses plasticity through the recruitment of GLUA2 AMPAR subunits,[10] a characteristic shared with GPC5. The neuronal factor PIRB also represses plasticity, and increased spine density has been found in these KO mice,[37] which is of relevance due to increased spine numbers at multisynaptic thalamocortical boutons in *Gpc5* cKO mice. In the future, it will be important to determine whether GPC5 is actively repressing plasticity through direct regulation of synaptic stability or AMPAR subunit composition. Alternatively, increased plasticity in adulthood may be the result of incomplete circuit maturation and represent incomplete closure of the critical period in *Gpc5* cKO mice.

Identifying the mechanism of how astrocytic GPC5 regulates synapses will help elucidate how this molecule has a differential impact on thalamocortical and intracortical synapses. Our cell culture experiments demonstrated that soluble GPC5 protein is sufficient to induce the formation of presynaptic specializations without increasing terminal size or synapse numbers, suggesting that one type of action of GPC5 is presynaptic. Conversely, *in vivo* overexpression of GPC5 in *Gpc5* cKO mice is sufficient to increase levels of GLUA2 at intracortical synapses without impacting thalamocortical terminal size, suggesting a direct effect on postsynaptic sites. Identifying the neuronal receptor(s) through which GPC5 signals to regulate these distinct actions will give insight into these differences. Neuronal receptors for GPC family members include presynaptic PTPRD and PTPRS,[9,14,38] postsynaptic LRRTM4,[12,13] and postsynaptic GPR158.[38] In the hippocampus, neuronal GPC4 binds postsynaptic GPR158 to induce presynaptic differentiation, and loss of GPR158 leads to immature synaptic morphology specifically at mossy fiber synapses on CA3 neurons, similar to the thalamocortical phenotype in *Gpc5* cKO mice.[38] Future studies should investigate whether GPR158 or other candidate receptors are expressed by cortical neurons and responsible for mediating the effects of GPC5.

GPC5 can exist in a membrane-attached form via its GPI anchor, or be cleaved from the membrane and act in a soluble form in the extracellular space.[11] Previous studies of astrocyte GPC4 and GPC6 showed that they were functional in their cleaved form,[8] and in cell culture, soluble GPC5 protein is able to induce presynaptic specializations showing functionality. Determining the form of astrocytic GPC5 that is active in the brain will give insight into its mechanism of action. For example, both soluble and membrane-bound GPC4 regulate synaptogenesis through PTPRS, whereas only membrane-bound GPC4 can signal through GPR158.[9,14,38] This demonstrates that GPCs can have different mechanisms of action and receptor specificity depending on their form. This may explain why the remaining GPC5 expressed by OPCs is unable to compensate for loss of GPC5 in astrocytes, if, for example, membrane-bound GPC5 is the dominant form *in vivo* and requires close association between astrocyte processes and the synapse.

This study identifies astrocyte GPC5 as playing an important role in synapse maturation. We show that GPC5 is necessary for refinement and strengthening of thalamocortical synapses, and for functional maturation of intracortical synapses via recruitment of GLUA2 AMPA receptors. In humans, GPC5 dysregulation has been linked to multiple neurological disorders, including schizophrenia, Sanfilippo syndrome type B, Alzheimer's disease, frontotemporal dementia, and multiple sclerosis.[33–36,39–44] Our findings demonstrate that absence of GPC5 impacts synapse state and function, suggesting that further investigation of GPC5 is warranted in the neurological disorders where its level is decreased and synapses are dysfunctional.

Limitations of the study

To study the impact of astrocyte GPC5 on synapses, we generated an astrocyte-specific constitutive KO mouse model. We therefore cannot determine whether enhanced plasticity in adult cKO mice is due to an ongoing role of GPC5 or developmental circuit alterations. We focused our analysis on the impact of astrocyte GPC5 on neurons; however, we cannot discount the possibility that the observed synaptic changes are due to an alteration in astrocytes themselves (for example, in gene expression or morphology) that then impacts synapses. While GPC5 is expressed brain wide, our analysis focused on the VC, so further studies are needed to determine whether GPC5 has the same effect in other brain regions.

RESOURCE AVAILABILITY

Lead contact

Requests for further information and resources should be directed to and will be fulfilled by the lead contact, Nicola Allen (nallen@salk.edu).

Material availability

This study did not generate new unique reagents.

Data and code availability

- The EM datasets generated in this manuscript have been deposited at EMPIAR (EMPIAR: EMPIAR-12513) and are publicly available as of the date of publication. Accession numbers are listed in the key resources table.
- No original code was generated in this study.
- Any additional information required to reanalyze the data reported in this paper is available from the lead contact upon request.

STAR★METHODS

EXPERIMENTAL MODEL AND STUDY PARTICIPANT DETAILS

All animal experiments were approved by the Salk Institute IACUC.

Rats—Sprague-Dawley rats (Charles River stock number 001) were housed with a 12-h light/dark cycle in the Salk Institute animal facilities. Rats were provided access to food and water *ad libitum*. For astrocyte and neuron cell culture experiments, both sexes were used.

Mice—Mice were housed with a 12-h light/dark cycle in the Salk Institute animal facilities. Mice were provided access to food and water *ad libitum*. Mice of both sexes were used. Mice were analyzed at postnatal day (P28) during peak critical period, and at P120 (adult).

Astrocyte-specific Glypican 5 conditional knock out mice: To selectively remove *Gpc5* from astrocytes, *Gpc5 floxed* mice were crossed to *B6.Cg-Tg(Gfap-cre)73.12Mvs/J* (Jax 012886). *Gpc5 floxed* mice were generated by KOMP/MMRRC/EUCOMM as conditional ready mice. *Gpc5* strain was received as the tm1a allele (*C57BL/6N-Atm1Brd Gpc5tm1a(KOMP)Wtsi*, MMRRC Stock: 047921-UCD) and crossed with mice expressing *Flp recombinase* (*B6.129S4-Gt(ROSA)26Sortm1(FLP1)Dym/RainJ,* Jax 009086) to generate *Gpc5tm1c(KOMP)Wtsi* (UC Davis KOMP repository, project ID CSD76974). All experiments were performed using *Gpc5 flox/flox cre negative* (WT) and *cre positive* (cKO) littermates.

METHOD DETAILS

Tissue collection and preparation—Mice were anesthetized with an intraperitoneal injection of 100 mg/kg Ketamine (Victor Medical Company) and 20 mg/kg Xylazine (Anased) prior to intracardial perfusion. For collection of fresh frozen tissue used for single molecule fluorescent *in situ* hybridization (smFISH) experiments, mice were transcardially perfused with 10 mls PBS. Collected brains were embedded in OCT (Scigen 4583), frozen in dry ice/ethanol, and stored at −80°C. For collection of fixed brains used for immunohistochemistry experiments, mice were transcardially perfused with 10 mls PBS followed by 10 mls 4% PFA. Collected brains were placed in 4% PFA overnight at 4°C, washed 3 times in PBS, and cryoprotected in 30% sucrose at 4°C before being embedded in TFM (General data healthcare TFM-5), frozen in dry ice/ethanol and stored at −80°C. For cell fill experiments, mice were transcardially perfused with oxygenated aCSF (in mM: NaCl 126, $NaHCO_3$ 26, Glucose 10, KCl 2.5, $MgCl_2$ 2, NaH_2PO_4 1.25, $CaCl_2$ 2, pH 7.4) at 34°C for 30 s followed by 34°C 4% PFA for 15 min. Brains were collected and immediately sectioned on a vibratome. For electron microscopy (EM) experiments, mice were transcardially perfused with oxygenated aCSF (in mM: NaCl 126, $NaHCO_3$ 26, Glucose 10, KCl 2.5, $MgCl_2$ 2, NaH_2PO_4 1.25, $CaCl_2$ 2, pH 7.4) with 20U/mL Heparin (Sigma Aldrich H3393) at 34°C for 30 s followed by 75 mls of 0.15 M Cacodylate buffer, 2.5% Glutaraldehyde, 2% PFA, 4mM $CaCl_2$ warmed to 37°C. Brains were collected and stored overnight at 4°C in 0.15 M Cacodylate buffer, 2.5% Glutaraldehyde, 2% PFA, 4mM $CaCl_2$. Prior to sectioning on a vibratome, brains were washed three times in ice-cold 0.15M Cacodylate buffer with 4mM $CaCl_2$.

Single molecule fluorescent *in situ* hybridization (smFISH)—*Gpc5* WT and cKO littermate mice were used at P28 to analyze *Gpc5* cell-type expression (astrocyte, neuron, OPC) and efficiency of *Gpc5* removal from astrocytes, and to determine if *Gpc5* removal

impacts expression of *Gpc4*, *Gpc6* or *Chrdl1*, and at P28 and P120 to analyze *Arc* expression in the BZ of VC following monocular enucleation.

RNAscope version 1 protocol—Fresh frozen, 18 μm coronal sections (3.4 mm posterior to bregma) were obtained using a cryostat (Hacker Industries OTF5000). smFISH RNAscope (ACDbio 320850) was performed following manufacturer's instructions for fresh frozen tissue. Slides were frozen at −20C for 20 min, followed by 15 min in 4% PFA at 4C. Sections then underwent dehydration via 5 min washes in 50%, 75%, and 100% (x2) ethanol. Following dehydration, sections were incubated with Protease 3 (P28) or Protease 4 (P120) for 15 min at room temperature and then washed 2 times in PBS. Slides were incubated with target probes for 2 h at 40C followed by 3 amplification steps and 1 detection step with RNAscope wash buffer rinses between each step. Sections were mounted with SlowFade gold antifade with DAPI (Thermo Fisher S36939) and coverslip applied (22 mm × 50 mm, 1.5 thickness) and sealed with clear nail polish. Slides were imaged within 1 day or stored at −20C.

Probes used were *Gpc4* (ACDbio 442821), *Gpc5* (ACDbio 442831), *Gpc6* (ACDbio 453301), *Slc1a3*/GLAST (ACDBio 430781-C2), *Cspg4* (ACDbio 404131-C3), and *Arc* (ACDbio 316911). A negative 3-plex probe (ACDbio 320871) was used as a negative control to determine the level of background signal. Probes for *Gpc4, Gpc5, Gpc6* and *Arc* were imaged in channel 550; *Slc1a3*/GLAST was imaged in channel 488; *Cspg4* was imaged in channel 647.

To determine glypican expression layers 1 to 6 of the VC were imaged using a 203 objective on a Zeiss LSM710 confocal microscope at 2048x2048 pixels as 2μm z-stacks (3 slices). Representative images are maximum intensity projections of the z stack. Quantification of smFISH signal was performed using an ImageJ macro.[15] Images were made into maximum intensity projections and astrocytes and OPCs identified by their respective probes, with a region of interest (ROI) drawn around each astrocyte or OPC cell body. The probe of interest (*Gpc4*, *Gpc5* or *Gpc6*) channel was thresholded in the same way for all images, cell-type ROIs were applied, and the thresholded area of probe signal recorded for each ROI. A minimum of 5 littermate pairs of mice, and 3 sections per mouse were imaged. Data in graphs presented as average per mouse.

For *Arc* experiments entire coronal sections containing the BZ of VC were imaged with a 10× objective, as 16-bit images on a Zeiss Axio Imager.Z2 fluorescent microscope with 10% tile overlap. A minimum of 5 littermate pairs of mice, and 4 sections per mouse were imaged. Data in graphs presented as average per mouse.

RNAscope version 2 protocol—PFA fixed 18 μm coronal sections (3.4 mm posterior to bregma) were obtained using a cryostat (Hacker Industries OTF5000). smFISH RNAscope (ACDbio 323110) was performed following manufacturer's instructions for fixed tissue. Slides were washed with PBS, followed by 15 min in 4% PFA at 4C. Sections then underwent dehydration via 5 min washes in 50%, 75%, and 100% (x2) ethanol. Following dehydration, hydrogen peroxide was applied to the sections for 10 min at room temperature and washed with molecular grade water (2x), sections were then incubated with Protease

3 for 15 min at room temperature and washed with PBS (2X). Slides were incubated with target probes for 2 h at 40C followed by 3 amplification steps, then horseradish peroxidase (HRP), then dye of choice, and finally HRP blocker, with 2 RNAscope wash buffer rinses between each step.

RNAscope was followed by immunostaining for S100beta (Abcam AB52642-1001) as an astrocyte marker. After HRP blocker step of RNAscope, the sections were incubated in blocking serum with 10% goat serum, 90% PBS and 0.2% Triton for 1 h. S100b rabbit primary antibody was added at 1:500 in serum (5% goat serum, 95% PBS, 0.2% Triton) and left overnight at 4C. Alexa Fluor goat anti-rabbit 488 (Invitrogen A11034) secondary antibody was added at 1:500 in serum and sections were incubated for 2 h at room temperature. 1:1000 DAPI in PBS was added to sections for 5 min and mounted with Fluoromount-G media (SouthernBiotech 0100-01), and coverslip applied (22 mm × 50 mm, 1.5 thickness) and left to dry for 1 h. Slides were stored at −20C and imaged within 1 week.

Probes used were *Gpc5* (ACDbio 442831), *Tubb3* (ACDbio 423391-C3), and *Chrdl1* (ACDbio 442811). Probes for *Gpc5* and *Chrdl1* were imaged in channel 550, and *Tubb3* in channel 647; S100b was imaged in channel 488. The sections were imaged using a Zeiss LSM 900 confocal microscope, as z stack at 1um intervals (8-10 slices). Representative images are maximum intensity projection of the z stack. Analysis was performed as described under RNAscope version 1.

Immunohistochemistry and synaptic puncta analysis—Littermate pairs of *Gpc5* WT and cKO mice were used for immunohistochemistry experiments at P28 and P120. Coronal sections (20mm) containing the BZ of VC were cut from PFA fixed mouse brains on a cryostat, mounted on Superfrost Plus micro slides (VWR 48311-703), and immediately processed for immunohistochemistry. Sections were placed in an RT humidified chamber to be blocked and permeabilized for 1 h in 5% goat serum and 0.3% Triton X-100 in PBS. Sections were incubated with primary anti-bodies in a humidified chamber overnight at 4°C. Primary antibodies were diluted in 5% goat serum, 0.3% Triton X-100, and 100mM lysine in PBS. Primary antibodies used: rabbit anti-GLUA1 (Millipore AB1504) 1:500; rabbit anti-GLUA2 (Millipore AB1768-I) 1:500; guinea pig anti-VGLUT1 (Millipore AB5905) 1:1000; guinea pig anti-VGLUT2 (Millipore AB2251) 1:1000. Sections were washed 3 × 5 minutes in PBS, then incubated with secondary antibodies in a humidified chamber at RT for 2 h. Secondary antibodies were diluted in 5% goat serum, 0.3% Triton X-100, and 100mM lysine in PBS. Secondary antibodies used: goat anti-rabbit Alexa 488 (Thermo Fisher Scientific A11034) 1:500; goat anti-guinea pig Alexa 594 (Thermo Fisher Scientific A11076) 1:500. Sections were incubated with secondary antibodies alone as a negative control. Sections were washed 3 × 5 minutes with PBS. SlowFade gold antifade mountant with DAPI (Thermo Fisher Scientific S36939) was applied to each section and a coverslip (22 mm × 50 mm 1.5 thickness) placed on top and sealed with clear nail polish.

Images were acquired on a Zeiss LSM-880 confocal microscope using a 63× oil immersion objective (1.4NA) as 16-bit images, 1420x1420 pixels, 0.08μm × 0.08μm pixel size, as a z stack of 8 slices with a total thickness of 2.68μm. For VGLUT1 and GLUA1/2 co-staining images were taken in VC L1 and L2/3. For VGLUT2 and GLUA1/2 co-staining images

were taken in VC L1 and L4. Imaging conditions were determined based on the WT condition and applied to the cKO acquired in the same session.

Synaptic staining images were analyzed using IMARIS software (Bitplane) to determine individual puncta number (VGLUT, GLUA) and synapse number (colocalized VGLUT and GLUA). Four 25μm × 25μm ROIs were selected from within each image for analysis. Each z stack was viewed as a 3D image and a Gaussian filter of 0.0725μm applied. Puncta were selected by manually thresholding the image and defined using the spots tool as spheres with a set diameter: GLUA1 0.4μm, GLUA2 0.4μm, VGLUT1 0.4μm, VGLUT2 0.5μm. Synapses were defined as colocalization of presynaptic puncta (VGLUT1 or VGLUT2) and postsynaptic puncta (GLUA1 or GLUA2) using the spots colocalization function, measuring a distance of 0.7μm from center to center of each spot. Volume of VGLUT2 puncta was measured using the surface tool, thresholded to capture all puncta defined by the spots tool. All analysis was done blind to genotype. A minimum of 5 littermate pairs and 3 sections per animal were imaged and analyzed. Data in graphs presented as average per mouse. Example images are from a single confocal plane.

GPC5 injection and synaptic analysis—P14 littermate *Gpc5* cKO mice were injected with AAV2/5 virus expressing HA-GPC5 construct (described in[45]), or Lck-EGFP plasmid (Addgene #105598) for control conditions, under the control of astrocyte minimal promoter GfaABC1D. Mice were administered pre-operative carprofen (5 mg/kg) subcutaneously and anesthetized using isoflurane. The stereotaxic coordinates for visual cortex are 1 mm anterior and 2.5 mm lateral from lambda. Virus was injected bilaterally at 3 sites at a depth of 600 μm from the skull surface. The pipette was kept in the brain for 3 min after each injection to allow the virus to diffuse. Both HA-GPC5 and Lck-EGFP viruses were injected for a total titer of ~1×10^8 vg, with a maximum volume of 150nL per site. After injection, mice were sutured and placed back with the dam. Mice were monitored for 3 days post-surgery to ensure full recovery and were given a daily injection of carprofen (5 mg/kg).

Brains were collected at P28 (14 days postinjection) as described under ‘Tissue collection’, and prepared as described under ‘Immunohistochemistry’ with the following modifications. Brain sections were 18μm instead of 20 μm. Additional antibodies include primary rat anti-HA (Roche 11867423001) 1:100, rabbit anti-S100beta (Abcam AB52642-1001) 1:500, rabbit anti-GPC5 (ThermoFisher PA5-83490) 1:100; and secondary goat anti-rat Alexa 488 1:500, goat anti-rabbit Alexa 594 1:500. Sections were incubated with DAPI (Thermo Fisher Scientific 62247) for 10 min (1:1000), and Fluoromount-G (Southern Biotech 0100-01) was applied to each section and a coverslip (22 mm × 50 mm 1.5 thickness) placed on top.

Images were acquired on a Zeiss LSM-880 confocal microscope with the Airyscan mode using a 633 oil immersion objective (1.46NA) with a 1.8x digital zoom as 16-bit images, 1764x1764 pixels, 0.04μm × 0.04μm pixel size, as a z stack of 12 slices with a total thickness of 2.2μm. For VGLUT1-GLUA2 staining images were taken in VC L2/3. For VGLUT2 staining images were taken in VC L4. In both cases imaging was performed within the zone of astrocytes overexpressing either HA-Gpc5 or GFP identified by immunostaining. Imaging conditions were maintained across samples in an imaging session. Airyscan processed images were analyzed using Imaris software (9.9 version) to

determine VGLUT1 and GLUA2 puncta number and VGLUT2 puncta volume. Each z stack was viewed as a 3D image. GLUA2 and VGLUT1 puncta were selected by thresholding the image with threshold values maintained between GFP and HA-GPC5 conditions. Spots tool was used to identify puncta as spheres with a set diameter of 0.3μm. Synapses were defined as colocalization of presynaptic puncta (VGLUT1) and postsynaptic puncta (GLUA2) using the spots colocalization function, measuring a distance of 0.5μm from center to center of each spot. Volume of VGLUT2 puncta were measured using the surface tool with threshold values maintained between GFP and HA-GPC5 conditions. 5-6 mice per group and 3 sections per animal were imaged and analyzed. Data in graphs presented as average per mouse. Example images are from a single confocal plane.

Cell fills—Littermate pairs of *Gpc5* WT and cKO mice were used for experiments at P28. Coronal sections (200μm) of lightly PFA fixed tissue were cut on a vibratome in ice-cold PBS and stored in 4°C PBS for up to 48 h. Slices were placed in RT PBS on the stage of a Zeiss microscope, and pyramidal neurons in VC L2/3 identified and soma impaled with a sharp micropipette (100–400 MΩ) backfilled with 10mM Alexa 488 (Thermo Fisher A10436) in 200 mM KCl. Dye was injected by applying a 1.5 V negative pulse for 5–10 min until the cell was filled. After filling, slices were placed in 4°C 4% PFA for 30 min. Slices were mounted on slides with SlowFade gold antifade mountant with DAPI (Thermo Fisher Scientific S36939), coverslip applied (22 mm × 50 mm 1.5 thickness) and sealed with clear nail polish. Slides were prepared for slices by applying a thick clear nail polish boundary to prevent coverslips from crushing slices.

Images were acquired on a Zeiss LSM-880 confocal microscope using a 63× oil immersion objective as 16-bit, 1548 x 1548 pixel area, 0.08μm × 0.08μm pixel size images. Exposure parameters were established based on WT samples and all sections were imaged in a single session. A z stack (0.19μm step size) spanning the entire dendrite was taken for each cell, and both basal and apical secondary dendrites were imaged. Spine analysis was performed using NeuronStudio software.[46] A 15μm segment of secondary apical or basal dendrite was selected, at the first branchpoint, and the number of spines, spine neck length and spine head diameter were measured and classified according to.[47] A minimum of 5 littermate pairs of mice and 3 cells per mouse were imaged. Data in graphs presented as average per mouse.

APEX2 injection and electron microscopy—To label thalamocortical projections for EM reconstruction, AAV9-COX4-dAPEX2 was injected into the dLGN of WT and *Gpc5* cKO mice at P14 (2 littermate pairs). pAAV-COX4-dAPEX2 was a gift from David Ginty (Addgene plasmid #117176).[26] Packaging in AAV9 was performed by the Salk Viral Vector core facility (GT3) at a concentration of $2x10^{14}$ vg/mL. Mice were anesthetized with oxygenated isoflurane (2–3%) and injection was done with a Nanoject pressure injection system. Virus was diluted to $3x10^{12}$ vg/mL and injected at coordinates 2.0 mm posterior from bregma, 1.9 mm lateral from the midline, and 2.9 mm below the pia, with a total of 150nL of virus delivered at a rate of 2nL per second. Following 2 weeks of expression, mice were collected at P28 as described above and the brain was processed for electron microscopy as described with some modifications.[26,48] Materials used for processing samples for EM were sourced from Electron Microscopy Sciences unless

otherwise indicated. All steps were performed at ice-cold temperatures unless otherwise indicated.

Brains were mounted on a Leica VT1000S vibrating microtome in cacodylate buffer, and 100μm coronal sections containing the primary VC collected in 6 well plates and washed 2 × 10 min in cacodylate buffer supplemented with 50mM glycine, followed by 1 × 10 min in cacodylate buffer. A 10X diaminobenzidine (DAB) tetrahydrochloride solution was freshly prepared by dissolving 50mg of DAB in 0.1 M HCl at room temperature prior to tissue processing. Sections were then incubated in DAB solution (final concentration of 0.3 mg/mL DAB in cacodylate buffer) for 30 min in the dark. After 30 min, 10 μL/mL of cacodylate supplemented with 0.3% H_2O_2 was added directly to the DAB solution (final H_2O_2 concentration of 0.003%) and swirled extensively to initiate the peroxidase reaction which was allowed to proceed for 1 h in the dark. Slices were evaluated for reaction product and washed 3 × 10 min in cacodylate buffer and then further post-fixed overnight in cacodylate buffer with 3% glutaraldehyde.

The following day sections were rinsed 2 × 10 min in cacodylate buffer with 50mM glycine followed by 1 × 10 min in cacodylate buffer and transferred to a Petri dish filled with ice-cold cacodylate buffer for photography and microdissection. 2mm wide strips spanning from the cortical surface to the corpus collosum were collected into scintillation vials for further processing.

Samples were stained with reduced osmium (1% osmium tetroxide and 1.5% potassium ferrocyanide in cacodylate buffer) for 1h at room temperature, then rinsed 5 × 3 minutes with ice-cold water and left in 1% aqueous uranyl acetate at 4°C overnight. Samples were then serially dehydrated in ice-cold aqueous ethanol solutions of ascending concentrations, before 3 × 10 min incubations with absolute ethanol at room temperature. Samples were then infiltrated with ascending concentrations of Durcupan resin in absolute ethanol at room temperature (3:1, 4h; 1:1, 4h; 1:3, overnight) before 2 × 4h incubations rotating in pure resin. Samples were embedded with fresh resin and paper labels in silicon molds, with the tissue oriented *en face* to the block face and polymerized for 60 h at 65°C in an oven.

Serial sections were collected onto silicon wafers as described with some modifications.[49] Briefly, the block was trimmed using a 90° diamond trimming knife (Diatome) on an ultramicrotome (Leica UC7) to a trapezoidal frustum of roughly 150 × 400μm which included the region from the cortical surface to deep cortical layers. A silicon chip (35 × 7mm; University Wafer, Boston, MA) was hydrophilized in a plasma cleaner (Harrick) immediately preceding partial immersion in the water boat of a Histo knife (Diatome) mounted on the ultramicrotome. Ribbons of 150–200 serial sections of thicknesses of approximately 55nm were cut with 4 drops of pure ethanol in the water boat and an ionizing instrument (Leica EM Crion) activated and oriented toward the cutting edge of the knife from above. When ribbons of sufficient quality and length were generated, they were released from the knife edge using a single-eyelash brush and carefully positioned over the chip. The water level was then slowly lowered using a peristaltic pump, and sections were allowed to dry down on the silicon substrate. Chips were briefly dried on a slide on a hot plate set to 60°C.

Chips were mounted on aluminum stubs using carbon sticky tabs and loaded into a scanning electron microscope (SEM; Zeiss Sigma VP) equipped with a sensitive backscatter detector (Gatan), as well as extended raster scanning capabilities and a control system designed for serial section imaging workflows (ATLAS5, FIBICS). Low resolution image maps of the ribbon of serial sections were collected, and a mid-resolution map of a central section was generated for reference. From this image, a region of interest (ROI) from VC L4 of 50 × 50μm was selected from between 250 and 350μm from the cortical surface that [1] had DAB+ terminals; [2] was not obstructed by blood vessels or somata; [3] was free from obvious debris throughout the series as assessed from the low-resolution map. This region was identified at one end of the ribbon of sections, and the ROI was imaged at high resolution (pixel size: 2nm; dwell time: 6μs; EHT: 3kV; aperture: 30μm; working distance: 8-9mm) on every section in the ribbon.

Image stacks were collated and rigidly aligned using TrakEM2 in Fiji and cropped to a minimum continuous cube of roughly aligned data with minimal padding.[50] Fine stack alignment was accomplished using SWiFT-IR as deployed on 3DEM.org using the TACC compute resource Stampede 2.[51,52] The well aligned data was then imported into VAST Lite (VAST) for annotation and analysis.[53] Briefly, axons with DAB+ mitochondria and their corresponding postsynaptic partners were identified and manually segmented in VAST. Volume of terminals, vesicle cloud size, and PSD surface area were determined by individually segmenting structures and using VASTTOOLS MATLAB toolkit. To categorize post synaptic targets, all post synaptic structures synapsing with a target axonal terminal were segmented. 3D reconstructions of the segmented post synaptic structures were then determined to be either mushroom, thin, stubby, or shaft. Spines were categorized based on visual inspection of morphology. Mushroom spines were identified by the presence of a defined head and neck; thin spines were categorized as long filopodia like structures with no defined head; stubby spines were identified as short structures with no definable neck; shaft synapses occurred directly on the dendritic shaft. Data in graphs presented per presynaptic bouton or per postsynaptic spine. Visualizations of reconstructions were produced using the Neuromorph add-on in Blender 2.7 (Blender Foundation; blender.org).[54] Raw electron microscopy images are deposited at EMPIAR,[55] accession number EMPIAR-12513.

Electrophysiology—Coronal slices of primary visual cortex (V1) were prepared from WT and *Gpc5* cKO mice at P28-30. Animals were deeply anesthetized by injection with Avertin, decapitated, the brain removed, hemi-sected, and cut into 300 mm coronal sections using a Leica VT1000s vibratome in cold, sucrose-based dissection solution consisting of (in mM): 2.5 KCl, 7.0 $MgCl_2$, 1.25 Na_2HPO_4, 11 glucose, 234 sucrose, 0.5 $CaCl_2$, and 24 $NaHCO_3$ and equilibrated with carbogen (95% O_2/5% CO_2). Slices were placed in a recovery chamber containing artificial cerebrospinal fluid (aCSF) consisting of (in mM): 126 NaCl, 26 $NaHCO_3$, 1.25 Na_2HPO_4, 2.5 KCl, 2 $CaCl_2$, 1 $MgCl_2$, 25 glucose, and saturated with carbogen. Slices recovered for 30 min at 31°C and were maintained at room temperature until recordings were performed (up to 4–6 h).

Slices were placed in a recording chamber and perfused with a recirculating bath of carbogen-saturated aCSF at 31°C–33°C. Whole-cell patch clamp recordings were obtained from neurons in layer 2/3 of V1 visualized using IR-DIC on a Scientifica microscope. Open

pipette resistances were 2–5 MΩ (borosilicate glass pipette; Harvard Apparatus #30–0057). A potassium (K)-gluconate internal was used, consisting of (in mM): 115 K-gluconate, 20 KCl, 10 phosphocreatine disodium salt, 10 HEPES acid, 0.2 EGTA, 4 Mg-ATP, and 0.3 Na-GTP; osmolarity and pH were adjusted to 290–310 mOsm and pH 7.3–7.4 with double-distilled water and KOH. 100 μM spermine tetrahydrochloride (Tocris #0958) was added to the internal solution to maintain the physiological intracellular blockade of calcium-permeable GLUA2 lacking AMPARs at hyperpolarized potentials. Recordings were performed using a Multiclamp 700B amplifier (Molecular Devices, Sunnyvale, CA) and acquired in pClamp software. Data were filtered at 2 kHz and sampled at 10 kHz. Recordings were discarded if the series resistances were >25 MΩ or changed >25% during the entire recording. For recording AMPAR-mediated spontaneous excitatory postsynaptic currents (sEPSCs), aCSF contained 40 μM bicuculline methochloride (Tocris #0131) and 50 μM D-AP5 (Tocris #0106).

sEPSC recordings were filtered post-hoc with a 1 kHz low-pass Bessel 8-pole filter in Clampfit (Molecular Devices). Offline data analyses were performed using MiniAnalysis (Synaptosoft), as previously described.[10]

Monocular enucleation and *Arc* analysis—Littermate pairs of *Gpc5* WT and cKO mice were used for experiments at P28 (critical period) and P120 (adult). Mice were anesthetized with 2% isoflurane in oxygen and the right eye was removed via transection of the optic nerve. The empty ocular cavity was filled with Gelfoam (Pfizer 031508) and eyelid was sutured closed with 6-0 silk sutures (Henry Schein 101-2636). Erthromycin 0.5% and lidocaine 2% were applied to sutured eyelid. Overnight deprivation (control) mice were collected 12 hours later. 5-day monocularly deprived mice were collected after 5 days. Mice were maintained in a 12-hour light/12-hour dark cycle and collected (as described above) at the end of a 12-hour dark cycle. Mice were exposed to 30 min of bright light to induce *Arc* expression in neurons in the VC stimulated by the open eye before tissue collection. Coronal sections (18μm) were made from fresh frozen tissue on a cryostat and smFISH for *Arc* and imaging performed as described above. The width of the activated binocular zone was measured by analyzing the width of the *Arc* signal in VC L2/3 contralateral to the deprived eye performed using the measure tool in Zen blue edition software (Zeiss). A minimum of 5 littermate pairs and 4 sections per mouse were analyzed. Data in graphs presented as average per mouse.

Cell culture

Retinal ganglion cell neuron culture—Retinal ganglion cell neurons (RGCs) were isolated from P5-P7 Sprague-Dawley rat retinas using immunopanning as described.[9,56] Cells were plated at a density of 30,000 cells/well on glass coverslips (12mm diameter, Carolina Biological Supply 633029) treated with poly-D-lysine (Sigma P6407) and laminin (R&D 340001001) and grown in 24-well plates. RGCs were cultured in growth media containing: 50% DMEM (Thermo Fisher 11960044), 50% Neurobasal (Thermo Fisher 21103049), Penicillin-Streptomycin (Thermo Fisher 10437028), Glutamax (Thermo Fisher 35050-061), sodium pyruvate (Thermo Fisher 11360-070), N-acetyl-L-cysteine (Sigma A8199), insulin (Sigma I1882), triiodo-thyronine (Sigma T6397), SATO (containing:

transferrin (Sigma T-1147), BSA (Sigma A-4161), progesterone (Sigma P6149), putrescine (Sigma P5780), sodium selenite (Sigma S9133)), B27 (Thermo Fisher 17504044), BDNF (Pe-protech 450-02), CNTF (Peprotech 450-13), and forskolin (Sigma F6886). RGCs were cultured in a humidified incubator at 37°C and 10% CO_2 with a half-media change every 3 days.

Cortical astrocyte culture—Cortical astrocytes were isolated and cultured as described from P1-P2 Sprague-Dawley rats.[15,57] After isolation astrocytes were plated in 15cm cell culture plates coated with poly-D-lysine (Sigma P6407) at 3 million cells/plate and maintained at 37°C and 10% CO2. Astrocyte culture medium was DMEM (Thermo Fisher 11960044) with 10% heat-inactivated fetal bovine serum (Thermo Fisher 10437028), Penicillin-Streptomycin (Thermo Fisher 10437028), Glutamax (Thermo Fisher 35050-061), insulin (Sigma I1882), sodium pyruvate (Thermo Fisher 11360-070), hydrocortisone (Sigma H0888), N-acetyl-L-cysteine (Sigma A8199). For RGC feeder layer treatment astrocytes were plated on cell culture inserts for use in a 24-well plate (Thermo Fisher 353104) at 50,000 cells/insert. Before addition to wells containing RGCs, inserts were washed 3 x with 34°C DPBS to remove astrocyte growth medium and switched to RGC growth medium.

RGC neuron treatment—RGCs were cultured for 7–10 days in full RGC growth media to allow neurite outgrowth, prior to treatment for 6 days with astrocytes or purified GPC5. There were 3 conditions: RGCs alone (negative control), RGCs with a feeder layer of astrocytes (positive control), RGCs + recombinant mouse GPC5 at 1 μg/ml (R&D 2689-G5-050/CF, resuspended in DPBS at 0.1μg/μL).

Synaptic staining cultured RGC neurons—RGCs were washed 3 × 5 min with 34°C DPBS, fixed in 4% PFA at 34°C for 10 min, washed 3 × 5 min in PBS, blocked and permea-bilized for 30 min at RT in 50% antibody buffer (NaCl 150mM, Tris Base 50 mM, BSA 1%, L-Lysine 100 mM), 50% goat serum, and 0.2% Triton X-100, washed 1 × 5 min with PBS. Primary antibodies were diluted in antibody buffer with 10% goat serum and incubated over night at 4°C: mouse anti-PSD95 (Thermo Fisher MA1-045) 1:500, rabbit anti-VGLUT2 (Synaptic Systems 135–403) 1:1000. The next day RGCs were washed 3 × 5 min with PBS and incubated with secondary antibodies: goat anti-mouse Alexa 488 (Thermo Fisher A11029) 1:1000, and goat anti-rabbit Alexa 594 (Thermo Fisher A11037) 1:1000 at RT for 1 h, washed 3 × 5 min with PBS and coverslips mounted on microscope slides (Fisherfinest 12-544-2) with SlowFade gold antifade mountant with DAPI (Thermo Fisher S36939) and sealed with clear nail polish.

RGCs were imaged on a Zeiss AxioImager.Z2 microscope with a 633 oil immersion objective. Images were acquired at 14 bit, 1388x1040 image size, pixel size 0.102μm × 0.102μm. RGCs were selected in the DAPI (nucleus) channel, then pre and postsynaptic puncta imaged. Exposure settings for each imaging session were established based on the positive control (+astrocytes) and used for each image. Synaptic analysis was carried out using the ImageJ (NIH) puncta analyzer plug-in as previously described.[8,58] Briefly, thresholds to select pre and postsynaptic puncta were established using the positive control condition (+astrocytes), then applied to all images to select puncta to be considered for colocalization = synapse. VGLUT2 puncta size analysis was carried out in ImageJ.

Images of the VGLUT2 channel were thresholded based on the positive control condition (+astrocytes), then the 'analyze particles' function used to select thresholded puncta and measure their area. Two or three coverslips per condition and 10 cells per coverslip were imaged, giving 20–30 cells per group per experiment, and the experiment was repeated on 4 separate cultures. Data are presented as combined cells from all 4 experiments, and within each experiment data are normalized to the RGC alone condition.

QUANTIFICATION AND STATISTICAL ANALYSIS

Data in graphs is presented as mean ± S.E.M. along with individual data points representing mice or cells as indicated in the figure legend. Statistical analysis was performed with Prism and the test used indicated in the figure legend. All tests were 2-tailed, and exact *p* values are reported on the graph. Data were tested for normality of distribution before statistical testing. For 2 samples an unpaired T test was used for normally distributed data and a Mann-Whitney test for non-normally distributed data. For more than 2 samples an ANOVA with Tukey's post-hoc test for multiple comparisons was used for normally distributed data, and a Kruskal-Wallis ANOVA on ranks with Dunn's post-hoc test for multiple comparisons used for non-normally distributed data. To compare categories a Chi-square test was used.

Supplementary Material

Refer to Web version on PubMed Central for supplementary material.

ACKNOWLEDGMENTS

We thank Cari Dowling and Joseph Hash for technical assistance, Alison Caldwell for initial GPC5 experiments, and Casey Peto for pilot EM experiments. Work was supported by NIH-NINDS R01 NS089791, the Pew Foundation, and the CZI Neurodegeneration Network (to N.J.A.). U.M. is supported by an NSF NeuroNex Award (2014862) and the Chan-Zuckerberg Initiative Imaging Scientist Award. M.C. is supported by a Ford Foundation Predoctoral Fellowship. L.S. is supported by NIH-NEI F32 EY033629. I.H.S. is supported by fellowships from the Bright Focus Foundation and Alzheimer's Association. This work was supported by Salk Institute core facilities, including the GT3 Core Facility and the Waitt Advanced Biophotonics Core Facility, with funding from NIH-NCI CCSG P30 CA014195, NIH-NIA San Diego Nathan Shock Center P30 AG068635, The Henry L. Guenther Foundation, and the Waitt Foundation. Electron microscopy image processing was supported in part by NN1 NSF 1707356 and NN2 NSF 2014862. The authors acknowledge the Texas Advanced Computing Center (TACC) at The University of Texas at Austin for providing HPC and visualization resources. The graphical abstract was made in BioRender.

REFERENCES

1. Brill J, and Huguenard JR (2008). Sequential Changes in AMPA Receptor Targeting in the Developing Neocortical Excitatory Circuit. J. Neurosci 28, 13918–13928. 10.1523/jneurosci.3229-08.2008. [PubMed: 19091980]
2. Kumar SS, Bacci A, Kharazia V, and Huguenard JR (2002). A developmental switch of AMPA receptor subunits in neocortical pyramidal neurons. J. Neurosci 22, 3005–3015. [PubMed: 11943803]
3. Helm MS, Dankovich TM, Mandad S, Rammner B, Jähne S, Salimi V, Koerbs C, Leibrandt R, Urlaub H, Schikorski T, and Rizzoli SO (2021). A large-scale nanoscopy and biochemistry analysis of postsynaptic dendritic spines. Nat. Neurosci 24, 1151–1162. 10.1038/s41593-021-00874-w. [PubMed: 34168338]
4. Allen NJ, and Eroglu C (2017). Cell Biology of Astrocyte-Synapse Interactions. Neuron 96, 697–708. 10.1016/j.neuron.2017.09.056. [PubMed: 29096081]

5. Bosworth AP, and Allen NJ (2017). The diverse actions of astrocytes during synaptic development. Curr. Opin. Neurobiol 47, 38–43. 10.1016/j.conb.2017.08.017. [PubMed: 28938161]
6. Risher WC, Patel S, Kim IH, Uezu A, Bhagat S, Wilton DK, Pilaz LJ, Singh Alvarado J, Calhan OY, Silver DL, et al. (2014). Astrocytes refine cortical connectivity at dendritic spines. Elife 3, e04047. 10.7554/eLife.04047. [PubMed: 25517933]
7. Christopherson KS, Ullian EM, Stokes CCA, Mullowney CE, Hell JW, Agah A, Lawler J, Mosher DF, Bornstein P, and Barres BA (2005). Thrombospondins are astrocyte-secreted proteins that promote CNS synaptogenesis. Cellule 120, 421–433. 10.1016/j.cell.2004.12.020.
8. Allen NJ, Bennett ML, Foo LC, Wang GX, Chakraborty C, Smith SJ, and Barres BA (2012). Astrocyte glypicans 4 and 6 promote formation of excitatory synapses via GluA1 AMPA receptors. Nature 486, 410–414. 10.1038/nature11059. [PubMed: 22722203]
9. Farhy-Tselnicker I, van Casteren ACM, Lee A, Chang VT, Aricescu AR, and Allen NJ (2017). Astrocyte-Secreted Glypican 4 Regulates Release of Neuronal Pentraxin 1 from Axons to Induce Functional Synapse Formation. Neuron 96, 428–445.e13. 10.1016/j.neuron.2017.09.053. [PubMed: 29024665]
10. Blanco-Suarez E, Liu T-F, Kopelevich A, and Allen NJ (2018). Astrocyte-Secreted Chordin-like 1 Drives Synapse Maturation and Limits Plasticity by Increasing Synaptic GluA2 AMPA Receptors. Neuron 100, 1116–1132.e13. 10.1016/j.neuron.2018.09.043. [PubMed: 30344043]
11. Filmus J, Capurro M, and Rast J (2008). Glypicans. Genome Biol. 9, 224. 10.1186/gb-2008-9-5-224. [PubMed: 18505598]
12. Siddiqui TJ, Tari PK, Connor SA, Zhang P, Dobie FA, She K, Kawabe H, Wang YT, Brose N, and Craig AM (2013). An LRRTM4-HSPG complex mediates excitatory synapse development on dentate gyrus granule cells. Neuron 79, 680–695. 10.1016/j.neuron.2013.06.029. [PubMed: 23911104]
13. de Wit J, O'Sullivan ML, Savas JN, Condomitti G, Caccese MC, Vennekens KM, Yates JR 3rd, and Ghosh A (2013). Unbiased discovery of glypican as a receptor for LRRTM4 in regulating excitatory synapse development. Neuron 79, 696–711. 10.1016/j.neuron.2013.06.049. [PubMed: 23911103]
14. Ko JS, Pramanik G, Um JW, Shim JS, Lee D, Kim KH, Chung G-Y, Condomitti G, Kim HM, Kim H, et al. (2015). PTPσ functions as a presynaptic receptor for the glypican-4/LRRTM4 complex and is essential for excitatory synaptic transmission. Proc. Natl. Acad. Sci. USA 112, 1874–1879. 10.1073/pnas.1410138112. [PubMed: 25624497]
15. Farhy-Tselnicker I, Boisvert MM, Liu H, Dowling C, Erikson GA, Blanco-Suarez E, Farhy C, Shokhirev MN, Ecker JR, and Allen NJ (2021). Activity-dependent modulation of synapse-regulating genes in astrocytes. Elife 10, e70514. 10.7554/eLife.70514. [PubMed: 34494546]
16. Kaneko T, and Fujiyama F (2002). Complementary distribution of vesicular glutamate transporters in the central nervous system. Neurosci. Res 42, 243–250. 10.1016/S0168-0102(02)00009-3. [PubMed: 11985876]
17. Nahmani M, and Erisir A (2005). VGluT2 immunochemistry identifies thalamocortical terminals in layer 4 of adult and developing visual cortex. J. Comp. Neurol 484, 458–473. 10.1002/cne.20505. [PubMed: 15770654]
18. Dufour A, Rollenhagen A, Sätzler K, and Lübke JHR (2016). Development of Synaptic Boutons in Layer 4 of the Barrel Field of the Rat Somatosensory Cortex: A Quantitative Analysis. Cerebr. Cortex 26, 838–854. 10.1093/cercor/bhv270.
19. Oberlaender M, de Kock CPJ, Bruno RM, Ramirez A, Meyer HS, Dercksen VJ, Helmstaedter M, and Sakmann B (2012). Cell Type–Specific Three-Dimensional Structure of Thalamocortical Circuits in a Column of Rat Vibrissal Cortex. Cerebr. Cortex 22, 2375–2391. 10.1093/cercor/bhr317.
20. Rodriguez-Moreno J, Rollenhagen A, Arlandis J, Santuy A, Merchan-Pérez, A, DeFelipe J, Lübke JHR, and Clasca F (2018). Quantitative 3D Ultrastructure of Thalamocortical Synapses from the "Lemniscal" Ventral Posteromedial Nucleus in Mouse Barrel Cortex. Cerebr. Cortex 28, 3159–3175. 10.1093/cercor/bhx187.
21. Gu Y, and Cang J (2016). Binocular matching of thalamocortical and intracortical circuits in the mouse visual cortex. Elife 5, e22032. 10.7554/eLife.22032. [PubMed: 28033094]

22. Mizuno H, Luo W, Tarusawa E, Saito YM, Sato T, Yoshimura Y, Itohara S, and Iwasato T (2014). NMDAR-Regulated Dynamics of Layer 4 Neuronal Dendrites during Thalamocortical Reorganization in Neonates. Neuron 82, 365–379. 10.1016/j.neuron.2014.02.026. [PubMed: 24685175]

23. Zhang Y, Chen K, Sloan SA, Bennett ML, Scholze AR, O'Keeffe S, Phatnani HP, Guarnieri P, Caneda C, Ruderisch N, et al. (2014). An RNA-Sequencing Transcriptome and Splicing Database of Glia, Neurons, and Vascular Cells of the Cerebral Cortex. J. Neurosci 34, 11929–11947. 10.1523/jneurosci.1860-14.2014. [PubMed: 25186741]

24. Clarke LE, Liddelow SA, Chakraborty C, Münch AE, Heiman M, and Barres BA (2018). Normal aging induces A1-like astrocyte reactivity. Proc. Natl. Acad. Sci. USA 115, E1896–E1905. 10.1073/pnas.1800165115. [PubMed: 29437957]

25. Boisvert MM, Erikson GA, Shokhirev MN, and Allen NJ (2018). The Aging Astrocyte Transcriptome from Multiple Regions of the Mouse Brain. Cell Rep. 22, 269–285. 10.1016/j.celrep.2017.12.039. [PubMed: 29298427]

26. Zhang Q, Lee W-CA, Paul DL, and Ginty DD (2019). Multiplexed peroxidase-based electron microscopy labeling enables simultaneous visualization of multiple cell types. Nat. Neurosci 22, 828–839. 10.1038/s41593-019-0358-7. [PubMed: 30886406]

27. Harris KM, and Stevens JK (1988). Dendritic spines of rat cerebellar Purkinje cells: serial electron microscopy with reference to their biophysical characteristics. J. Neurosci 8, 4455–4469. 10.1523/jneurosci.08-12-04455.1988. [PubMed: 3199186]

28. Harris KM, and Stevens JK (1989). Dendritic spines of CA 1 pyramidal cells in the rat hippocampus: serial electron microscopy with reference to their biophysical characteristics. J. Neurosci 9, 2982–2997. 10.1523/jneurosci.09-08-02982.1989. [PubMed: 2769375]

29. Syken J, Grandpre T, Kanold PO, and Shatz CJ (2006). PirB restricts ocular-dominance plasticity in visual cortex. Science 313, 1795–1800. 10.1126/science.1128232. [PubMed: 16917027]

30. Bourne JN, and Harris KM (2008). Balancing Structure and Function at Hippocampal Dendritic Spines. Annu. Rev. Neurosci 31, 47–67. 10.1146/annurev.neuro.31.060407.125646. [PubMed: 18284372]

31. Knott GW, Holtmaat A, Wilbrecht L, Welker E, and Svoboda K (2006). Spine growth precedes synapse formation in the adult neocortex in vivo. Nat. Neurosci 9, 1117–1124. 10.1038/nn1747. [PubMed: 16892056]

32. Grillo FW, Song S, Teles-Grilo Ruivo LM, Huang L, Gao G, Knott GW, Maco B, Ferretti V, Thompson D, Little GE, and De Paola V (2013). Increased axonal bouton dynamics in the aging mouse cortex. Proc. Natl. Acad. Sci. USA 110, E1514–E1523. 10.1073/pnas.1218731110. [PubMed: 23542382]

33. Grubman A, Chew G, Ouyang JF, Sun G, Choo XY, McLean C, Simmons RK, Buckberry S, Vargas-Landin DB, Poppe D, et al. (2019). A single-cell atlas of entorhinal cortex from individuals with Alzheimer's disease reveals cell-type-specific gene expression regulation. Nat. Neurosci 22, 2087–2097. 10.1038/s41593-019-0539-4. [PubMed: 31768052]

34. Ling E, Nemesh J, Goldman M, Kamitaki N, Reed N, Handsaker RE, Genovese G, Vogelgsang JS, Gerges S, Kashin S, et al. (2024). A concerted neuron-astrocyte program declines in ageing and schizophrenia. Nature 627, 604–611. 10.1038/s41586-024-07109-5. [PubMed: 38448582]

35. Marsan E, Velmeshev D, Ramsey A, Patel RK, Zhang J, Koontz M, Andrews MG, de Majo M, Mora C, Blumenfeld J, et al. (2023). Astroglial toxicity promotes synaptic degeneration in the thalamocortical circuit in frontotemporal dementia with GRN mutations. J. Clin. Investig 133, e164919. 10.1172/JCI164919. [PubMed: 36602862]

36. Tsartsalis S, Sleven H, Fancy N, Wessely F, Smith AM, Willumsen N, Cheung TKD, Rokicki MJ, Chau V, Ifie E, et al. (2024). A single nuclear transcriptomic characterisation of mechanisms responsible for impaired angiogenesis and blood-brain barrier function in Alzheimer's disease. Nat. Commun 15, 2243. 10.1038/s41467-024-46630-z. [PubMed: 38472200]

37. Bochner DN, Sapp RW, Adelson JD, Zhang S, Lee H, Djurisic M, Syken J, Dan Y, and Shatz CJ (2014). Blocking PirB up-regulates spines and functional synapses to unlock visual cortical plasticity and facilitate recovery from amblyopia. Sci. Transl. Med 6, 258ra140. 10.1126/scitranslmed.3010157.

38. Condomitti G, Wierda KD, Schroeder A, Rubio SE, Vennekens KM, Orlandi C, Martemyanov KA, Gounko NV, Savas JN, and de Wit J (2018). An Input-Specific Orphan Receptor GPR158-HSPG Interaction Organizes Hippocampal Mossy Fiber-CA3 Synapses. Neuron 100, 201–215.e9. 10.1016/j.neuron.2018.08.038. [PubMed: 30290982]
39. Gandal MJ, Haney JR, Parikshak NN, Leppa V, Ramaswami G, Hartl C, Schork AJ, Appadurai V, Buil A, Werge TM, et al. (2018). Shared molecular neuropathology across major psychiatric disorders parallels polygenic overlap. Science 359, 693–697. 10.1126/science.aad6469. [PubMed: 29439242]
40. Irie F, Badie-Mahdavi H, and Yamaguchi Y (2012). Autism-like sociocommunicative deficits and stereotypies in mice lacking heparan sulfate. Proc. Natl. Acad. Sci. USA 109, 5052–5056. 10.1073/pnas.1117881109. [PubMed: 22411800]
41. Lau S-F, Cao H, Fu AKY, and Ip NY (2020). Single-nucleus transcriptome analysis reveals dysregulation of angiogenic endothelial cells and neuroprotective glia in Alzheimer's disease. Proc. Natl. Acad. Sci. USA 117, 25800–25809. 10.1073/pnas.2008762117. [PubMed: 32989152]
42. Potkin SG, Macciardi F, Guffanti G, Fallon JH, Wang Q, Turner JA, Lakatos A, Miles MF, Lander A, Vawter MP, and Xie X (2010). Identifying gene regulatory networks in schizophrenia. Neuroimage 53, 839–847. 10.1016/j.neuroimage.2010.06.036. [PubMed: 20600988]
43. Wang KS, Zhang Q, Liu X, Wu L, and Zeng M (2012). PKNOX2 is associated with formal thought disorder in schizophrenia: a meta-analysis of two genome-wide association studies. J. Mol. Neurosci 48, 265–272. 10.1007/s12031-012-9787-4. [PubMed: 22648509]
44. Schirmer L, Velmeshev D, Holmqvist S, Kaufmann M, Werneburg S, Jung D, Vistnes S, Stockley JH, Young A, Steindel M, et al. (2019). Neuronal vulnerability and multilineage diversity in multiple sclerosis. Nature 573, 75–82. 10.1038/s41586-019-1404-z. [PubMed: 31316211]
45. Salas IH, Paumier A, Tao T, Derevyanko A, Switzler C, Burgado J, Movsesian M, Metanat S, Dawoodtabar T, Asbell Q, et al. (2024). Astrocyte transcriptomic analysis identifies glypican 5 downregulation as a contributor to synaptic dysfunction in Alzheimer disease models. Preprint at bioRxiv. 10.1101/2024.10.30.621182.
46. Wearne SL, Rodriguez A, Ehlenberger DB, Rocher AB, Henderson SC, and Hof PR (2005). New techniques for imaging, digitization and analysis of three-dimensional neural morphology on multiple scales. Neuroscience 136, 661–680. 10.1016/j.neuroscience.2005.05.053. [PubMed: 16344143]
47. Risher WC, Ustunkaya T, Singh Alvarado J, and Eroglu C (2014). Rapid Golgi Analysis Method for Efficient and Unbiased Classification of Dendritic Spines. PLoS One 9, e107591. 10.1371/journal.pone.0107591. [PubMed: 25208214]
48. Martell JD, Deerinck TJ, Lam SS, Ellisman MH, and Ting AY (2017). Electron microscopy using the genetically encoded APEX2 tag in cultured mammalian cells. Nat. Protoc 12, 1792–1816. 10.1038/nprot.2017.065. [PubMed: 28796234]
49. Horstmann H, Körber C, Sätzler K, Aydin D, and Kuner T (2012). Serial Section Scanning Electron Microscopy (S3EM) on Silicon Wafers for Ultra-Structural Volume Imaging of Cells and Tissues. PLoS One 7, e35172. 10.1371/journal.pone.0035172. [PubMed: 22523574]
50. Cardona A, Saalfeld S, Schindelin J, Arganda-Carreras I, Preibisch S, Longair M, Tomancak P, Hartenstein V, and Douglas RJ (2012). TrakEM2 Software for Neural Circuit Reconstruction. PLoS One 7, e38011. 10.1371/journal.pone.0038011. [PubMed: 22723842]
51. Litvina E, Adams A, Barth A, Bruchez M, Carson J, Chung JE, Dupre KB, Frank LM, Gates KM, Harris KM, et al. (2019). BRAIN Initiative: Cutting-Edge Tools and Resources for the Community. J. Neurosci 39, 8275–8284. 10.1523/jneurosci.1169-19.2019. [PubMed: 31619497]
52. Wetzel AW, Bakal J, Dittrich M, Hildebrand DGC, Morgan JL, and Lichtman JW (2016). Registering large volume serial-section electron microscopy image sets for neural circuit reconstruction using FFT signal whitening. In 2016 IEEE Applied Imagery Pattern Recognition Workshop (AIPR) (IEEE), pp. 1–10.
53. Berger DR, Seung HS, and Lichtman JW (2018). VAST (Volume Annotation and Segmentation Tool): Efficient Manual and Semi-Automatic Labeling of Large 3D Image Stacks. Front. Neural Circ 12, 88. 10.3389/fncir.2018.00088.

54. Jorstad A, Blanc J, and Knott G (2018). NeuroMorph: A Software Toolset for 3D Analysis of Neurite Morphology and Connectivity. Front. Neuroanat 12, 59. 10.3389/fnana.2018.00059. [PubMed: 30083094]

55. Iudin A, Korir PK, Somasundharam S, Weyand S, Cattavitello C, Fonseca N, Salih O, Kleywegt GJ, and Patwardhan A (2023). EMPIAR: the Electron Microscopy Public Image Archive. Nucleic Acids Res. 51, D1503–D1511. 10.1093/nar/gkac1062. [PubMed: 36440762]

56. . Winzeler A, and Wang JT (2013). Purification and culture of retinal ganglion cells from rodents. Cold Spring Harb. Protoc 2013, 643–652. 10.1101/pdb.prot074906. [PubMed: 23818667]

57. McCarthy KD, and de Vellis J (1980). Preparation of separate astroglial and oligodendroglial cell cultures from rat cerebral tissue. J. Cell Biol 85, 890–902. 10.1083/jcb.85.3.890. [PubMed: 6248568]

58. Ippolito DM, and Eroglu C (2010). Quantifying Synapses: an Immunocytochemistry-based Assay to Quantify Synapse Number. J. Vis. Exp 2270, 2270. 10.3791/2270.

Highlights

- Astrocyte glypican 5 is necessary for cortical synapse maturation
- Glypican 5 regulates structural maturation of thalamocortical synapses
- Glypican 5 increases level of GluA2 AMPA receptors at intracortical synapses
- Lack of astrocyte glypican 5 increases adult neuronal plasticity

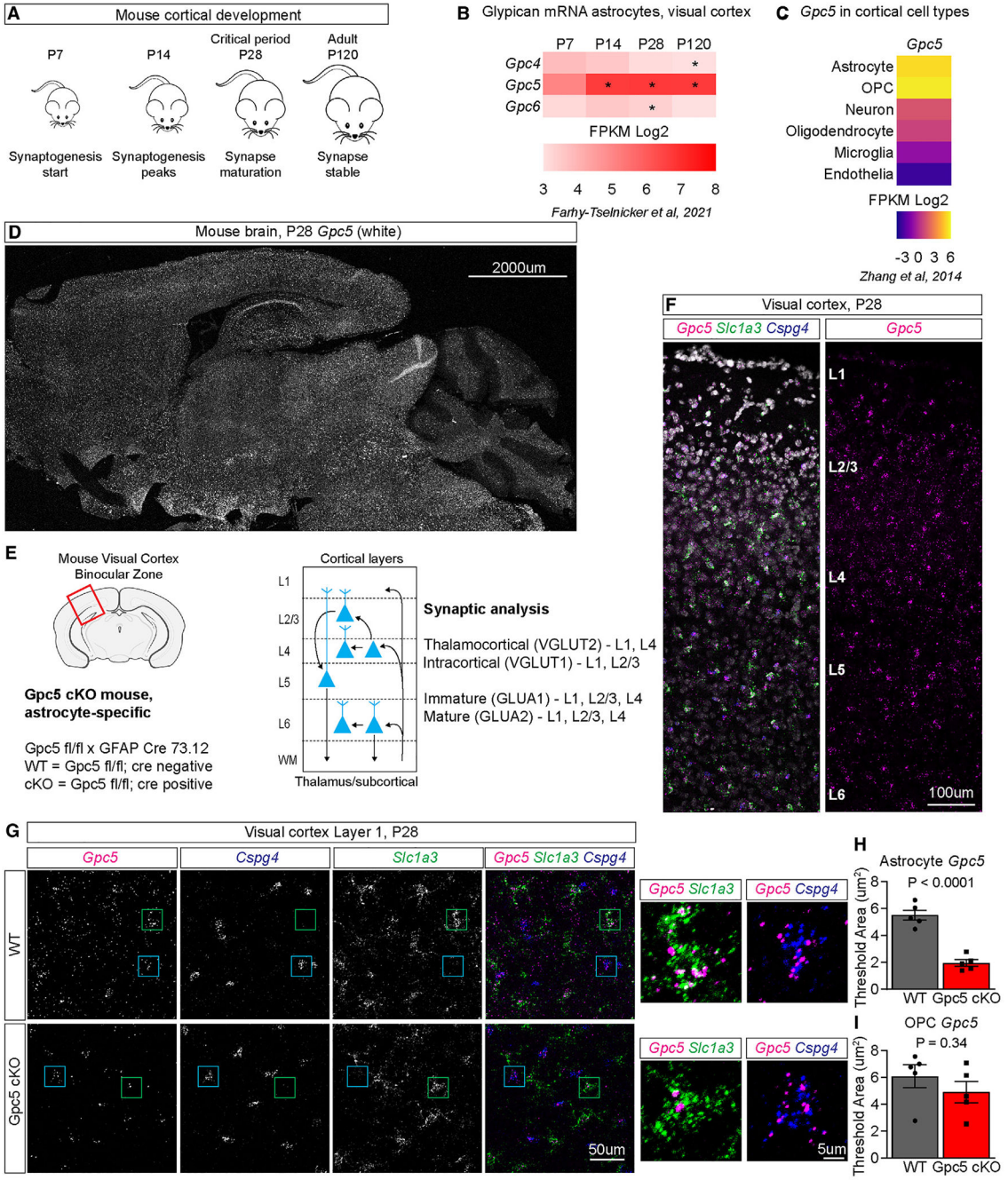

Figure 1. *Gpc5* is expressed throughout the brain by astrocytes and OPCs

(A) Mouse cortical synaptogenesis timeline.

(B) Expression of GPC mRNA by VC astrocytes across postnatal development. *Significantly altered vs. P7. Data are from Farhy-Tselnicker et al.[15]

(C) Cell type expression of *Gpc5* mRNA in the developing mouse cortex. Data are from Zhang et al.[23]

(D) *Gpc5* mRNA visualized using smFISH (WT brain, P28). Scale bar: 2,000 μm.

(E) *Gpc5* cKO mouse generation and experiment outline.

(F) *Gpc5* mRNA visualized using smFISH in astrocytes (*Slc1a3*) and OPCs (*Cspg4*) (VC, WT brain, P28). Scale bar: 100 μm.

(G–I) Validation of the *Gpc5* cKO mouse model.

(G) Representative images of WT and *Gpc5* cKO P28 VC *Gpc5* mRNA in L1 and colocalization with astrocytes (*Slc1a3*) and OPCs (*Cspg4*). Scale bar: 50 μm. Green box, magnification of an astrocyte; blue box, magnification of an OPC. Scale bar, magnified box: 5 μm.

(H and I) *Gpc5* mRNA expression in astrocytes (H) and OPCs (I) in cKO mice quantified across all cortical layers in the VC. $N = 5$ mice/condition. Graphs mean ± SEM, individual data points represent mice. Statistics: t test.

See also Figure S1.

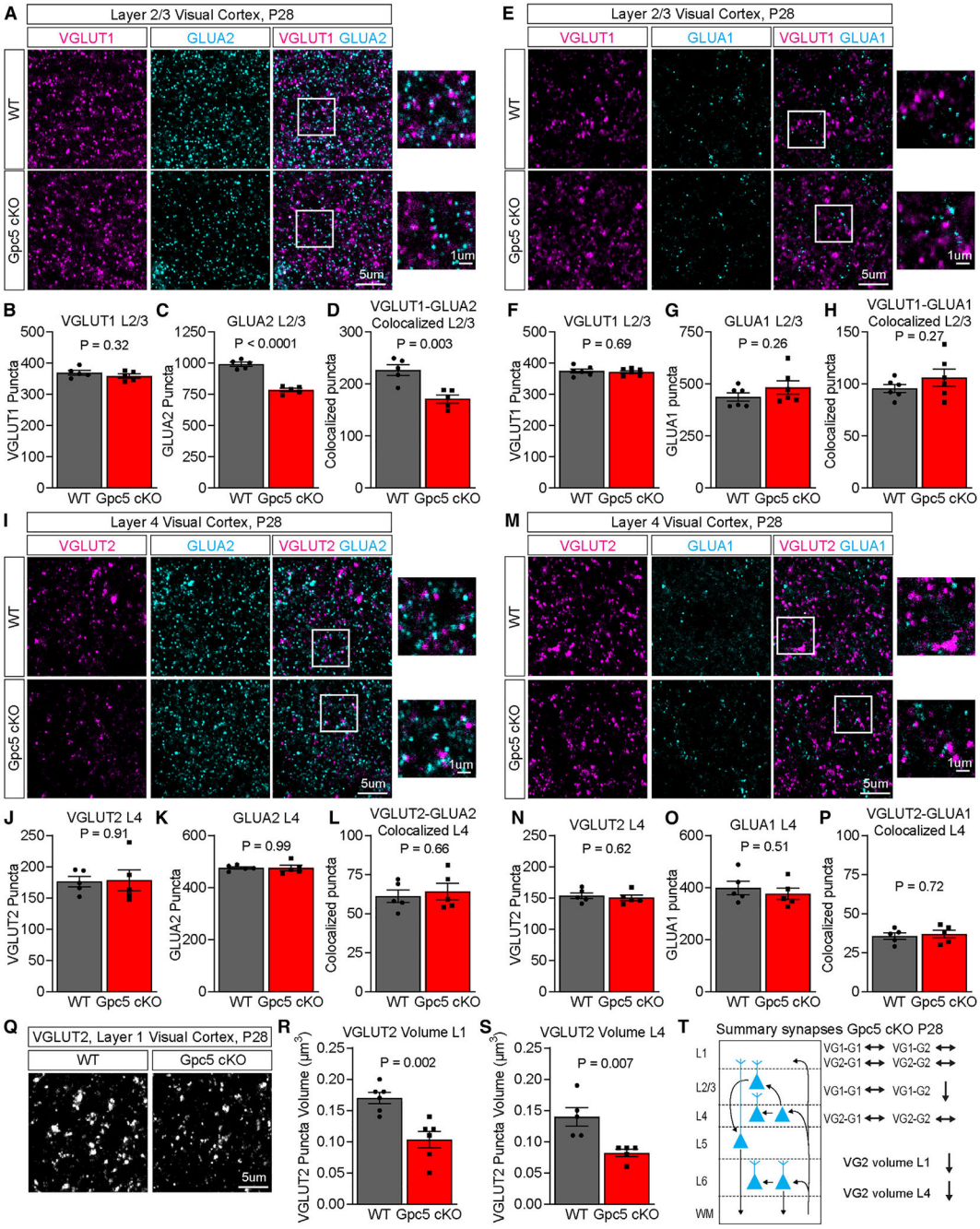

Figure 2. Synapses in *Gpc5* cKO mice are immature during the critical period

(A–D) GLUA2 protein level is decreased at intracortical synapses in *Gpc5* cKO mice at P28.

(A) Immunostaining of intracortical presynaptic VGLUT1 and postsynaptic GLUA2 in L2/3.

(B–D) Numbers of VGLUT1 (B), GLUA2 (C), and colocalized (D) puncta. $N = 5$ mice/condition.

(E–H) GLUA1 protein level is unchanged at intracortical synapses in *Gpc5* cKO mice at P28.

(E) Immunostaining of presynaptic VGLUT1 and postsynaptic GLUA1 in L2/3.

(F–H) Numbers of VGLUT1 (F), GLUA1 (G), and colocalized (H) puncta. $N = 6$ mice/condition.

(I–P) Thalamocortical synapses have unaltered AMPAR levels in *Gpc5* cKO mice at P28.

(I) Immunostaining of thalamocortical presynaptic VGLUT2 and postsynaptic GLUA2 in L4.

(J–L) Numbers of VGLUT2 (J), GLUA2 (K), and colocalized (L) puncta. $N = 5$ mice/condition.

(M) Immunostaining of thalamocortical presynaptic VGLUT2 and postsynaptic GLUA1 in L4.

(N–P) Numbers of VGLUT2 (N), GLUA1 (O), and colocalized (P) puncta. $N = 5$ mice/condition.

(Q–S) VGLUT2 puncta volume is decreased in P28 *Gpc5* cKO mice.

(Q) Immunostaining of VGLUT2 puncta in L1 VC.

(R and S) VGLUT2 puncta volume in L1 and L4. $N = 6$ mice/condition L1, $N = 5$ mice/condition L4.

(T) Summary of synaptic changes in *Gpc5* cKO mice at P28.

Scale bars: 5 μm (A, E, I, M, and Q, main) and 1 μm (A, E, I, and M, magnified). Graphs: mean ± SEM. Individual data points represent mice. Statistics: t test. See also Figure S2.

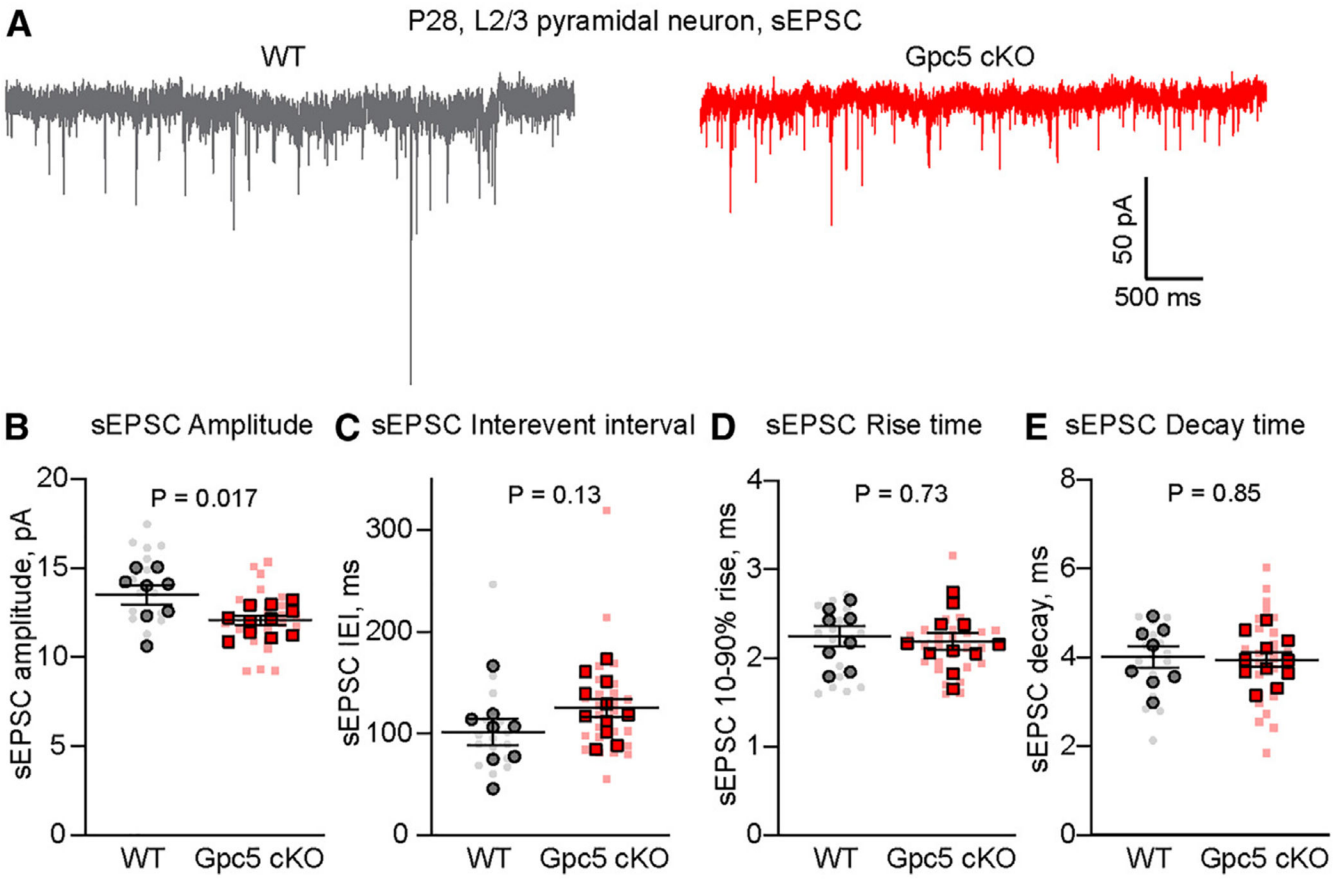

Figure 3. GPC5 regulates excitatory synapse strength

(A–E) Spontaneous excitatory postsynaptic currents (sEPSCs) are smaller in amplitude in L2/3 pyramidal neurons in *Gpc5* cKO mice at P28.

(A) Example recordings of sEPSCs from WT and Gpc5 cKO L2/3 pyramidal neurons.

(B–E) Quantification of sEPSC amplitude (B), interevent interval (C), 10%–90% rise time (D), and decay time (E).

Graphs: mean ± SEM. Large data points represent mouse averages and small data points cells. WT $n = 17$ cells from 8 mice, *Gpc5* cKO $n = 26$ cells from 11 mice. Statistics: t test on mouse averages.

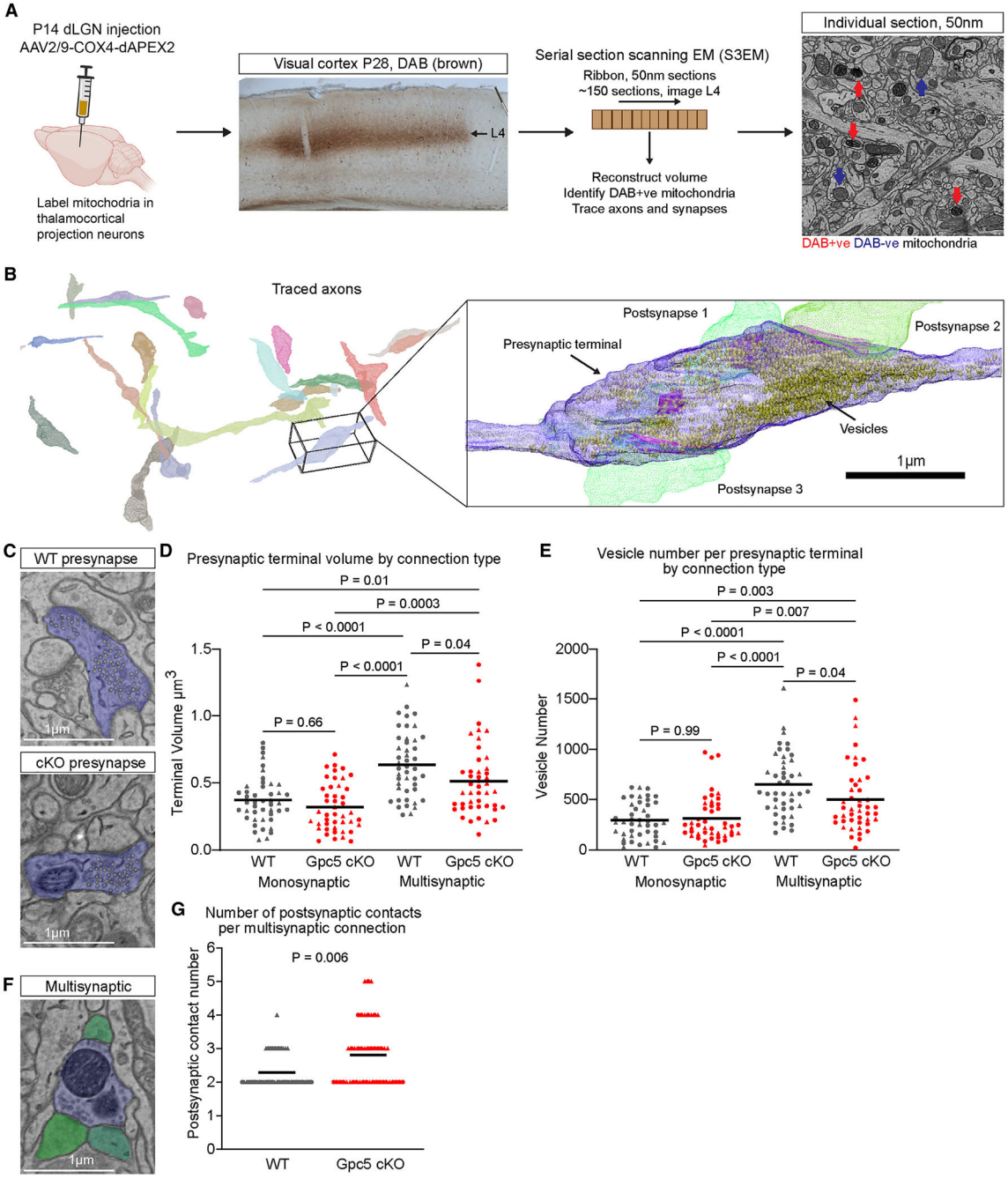

Figure 4. Thalamocortical synapses are structurally immature in *Gpc5* cKO mice

(A) Experiment overview.

(B) Reconstructed thalamocortical axons in L4. Magnification: presynaptic bouton and postsynaptic spines. Bouton, purple; vesicles, yellow; spines, green; PSD, magenta.

(C–E) Thalamocortical presynaptic boutons are smaller in *Gpc5* cKO mice.

(C) Example images. Vesicles, yellow; boutons, purple.

(D and E) Volume (D) and number of vesicles (E) in multisynaptic and monosynaptic thalamocortical axonal boutons in *Gpc5* cKO and WT mice. Statistics: two-way ANOVA.

(F and G) Postsynaptic contacts at multisynaptic thalamocortical boutons (F: presynaptic bouton, purple; postsynaptic spines, green) are increased in *Gpc5* cKO mice (G). Statistics: Mann-Whitney test.

Scale bars: 1 μm (B, C, and F). Graphs: mean. Data points represent boutons, and shape denotes donor mouse. $n = 45$ presynaptic boutons per condition from 2 mice per genotype. See also Figure S3 and Video S1.

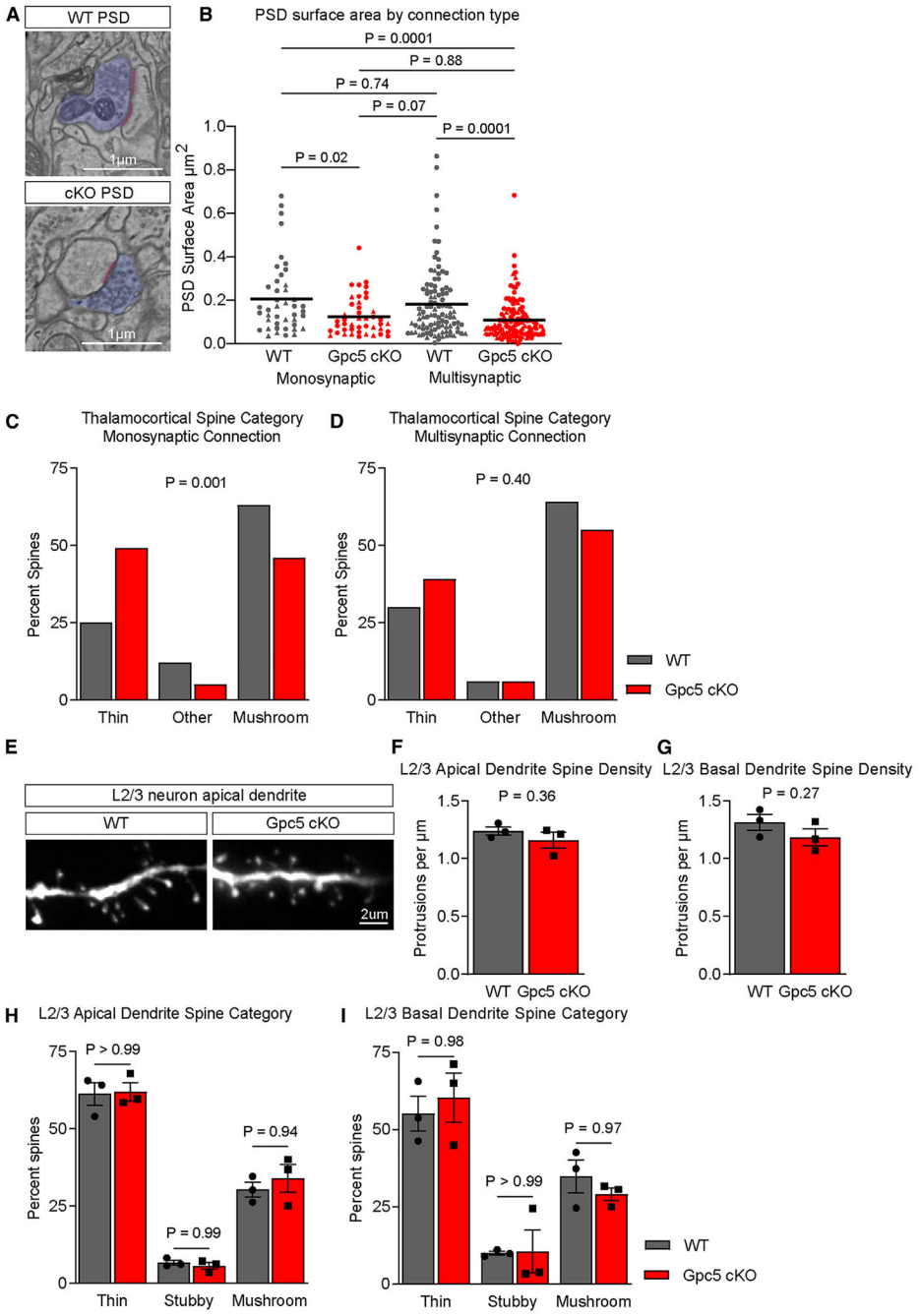

Figure 5. *Gpc5* cKO mice show altered postsynaptic structure at thalamocortical synapses

(A–D) Postsynaptic structures at L4 APEX2-positive thalamocortical synapses are immature in *Gpc5* cKO mice.

(A) Example images of PSDs in L4. PSD, magenta; axons, purple. Scale bar: 1 μm.

(B) PSD surface area. Graph: mean. Individual data points represent PSDs, and shape denotes donor mouse. $n = 45$ presynaptic boutons and associated PSDs per condition from 2 mice per genotype. Statistics: two-way ANOVA.

(C and D) Dendritic spine morphologies are shifted toward a more immature state in *Gpc5* cKO mice at monosynaptic (C) but not multisynaptic (D) APEX2-positive synapses. Statistics: chi-square test.

(E–I) No difference in dendritic spines of P28 L2/3 pyramidal cells in *Gpc5* cKO mice.

(E) P28 L2/3 pyramidal cell dendrites. Scale bar: 2 μm.

(F and G) Spine density of apical (F) and basal (G) dendrites.

(H and I) Spine shape of secondary apical (H) and basal (I) dendrites.

$N = 3$ mice. Graphs: mean ± SEM. Individual data points represent mice. Statistics: t test (F and G) and two-way ANOVA (H and I). See also Figure S4.

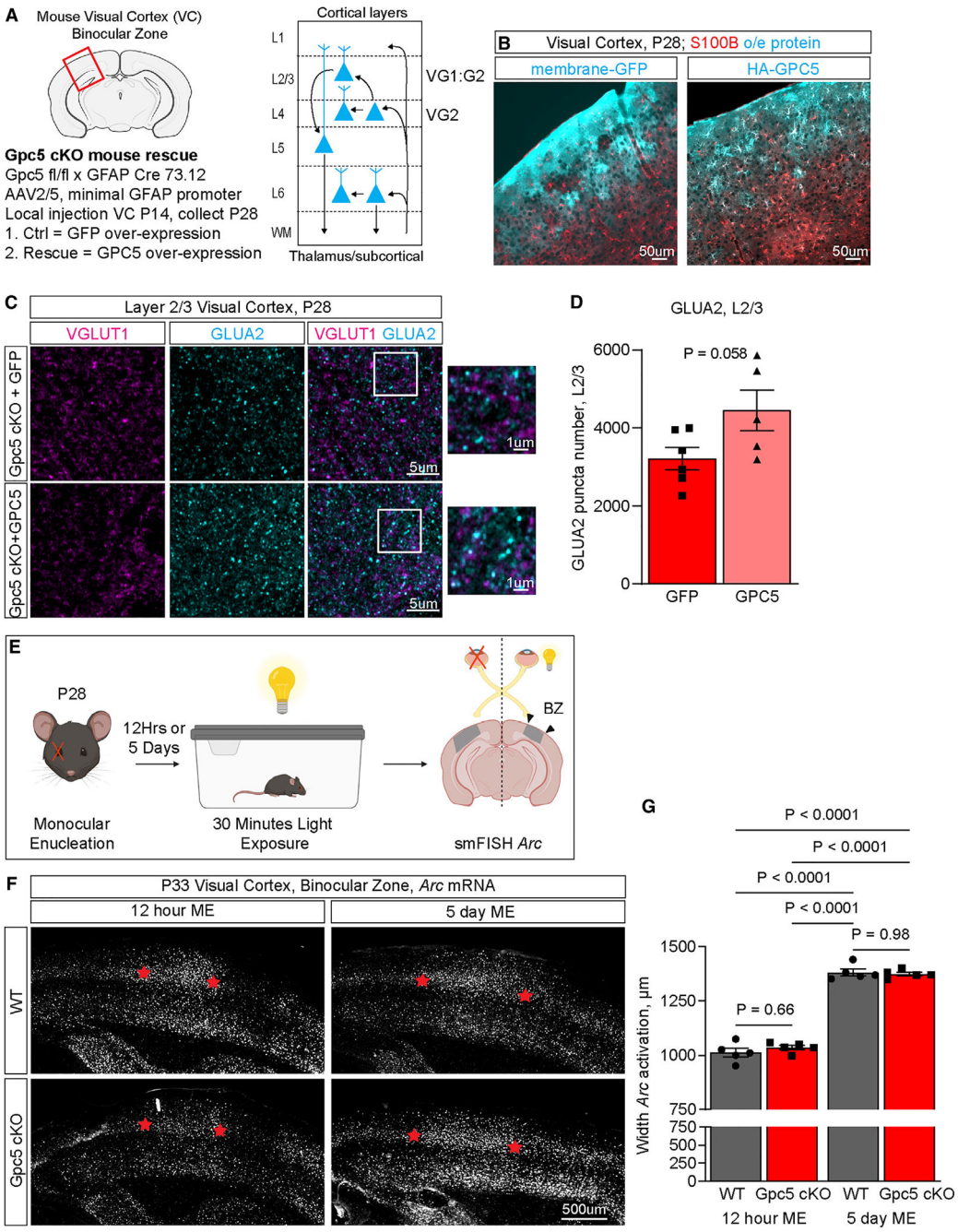

Figure 6. Impact of GPC5 on VC synapses during the critical period

(A–D) Overexpressing GPC5 in astrocytes in *Gpc5* cKO VC is sufficient to increase the GLUA2 level.

(A) Experimental design.

(B) Membrane-GFP or HA-GPC5 colocalize with the astrocyte marker S100beta. Scale bar: 50 µm.

(C) Immunostaining of intracortical presynaptic VGLUT1 and postsynaptic GLUA2 in L2/3. Scale bars: 5 µm (main) and 1 µm (magnified).

(D) Number of GLUA2 puncta. *N* = 5–6 mice/condition. Graph: mean ± SEM. Data points represent mice. Statistics: t test.

(E–G) Absence of GPC5 during the critical period does not impact large-scale remodeling in response to monocular enucleation (ME).

(E) Experiment overview

(F) *Arc* mRNA in the VC ipsilateral to the nondeprived eye 12 hours or 5 days after ME. Scale bar: 500 μm.

(G) Width of the binocular zone.

Graph: mean ± SEM. Individual points represent mice. *N* = 5 mice/condition. Statistics: two-way ANOVA. See also Figures S5 and S6.

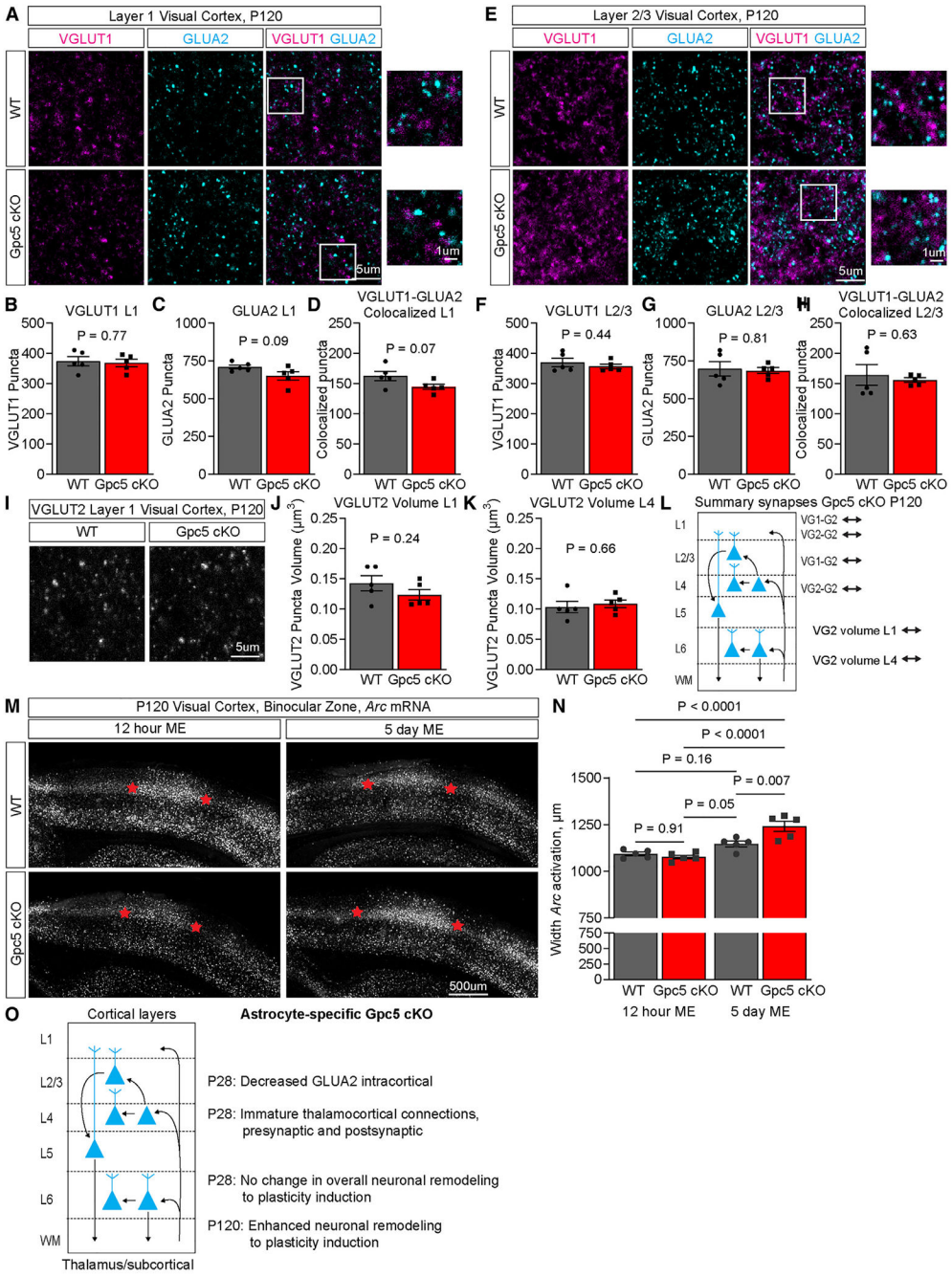

Figure 7. Impact of GPC5 on VC synapses in the adult

(A–H) GLUA2 puncta numbers are recovered at intracortical synapses in *Gpc5* cKO mice at P120.

(A and E) Immunostaining of intracortical presynaptic VGLUT1 and postsynaptic GLUA2 in L1 (A) and L2/3 (E).

(B–D and F–H) VGLUT1 (B and F), GLUA2 (C and G), and colocalized (D and H) puncta in L1 and L2/3.

(I–K) VGLUT2 puncta volume is recovered at P120 in *Gpc5* cKO mice.

(I) Immunostaining of VGLUT2 in layer 1 VC.
(J and K) VGLUT2 puncta volume in L1 (J) and L4 (K).
N = 5 mice/condition. Scale bars: 5 μm (A, E, and I, main) and 1 μm (A and E, magnified). Graphs: mean ± SEM. Individual points represent mice. Statistics: t test.
(L) Summary of synapse findings in *Gpc5* cKO mice at P120.
(M and N) Absence of astrocyte GPC5 enables enhanced ocular dominance plasticity in adulthood.
(M) *Arc* mRNA in the VC ipsilateral to the nondeprived eye 12 hours or 5 days after ME. Scale bar: 500 μm.
(N) Width of the binocular zone. Graph: mean ± SEM. Individual points represent mice. *N* = 5 mice/condition. Statistics: two-way ANOVA.
(O) Summary of phenotypes in *Gpc5* astrocyte-specific cKO mice.
See also Figure S7.

KEY RESOURCES TABLE

REAGENT or RESOURCE	SOURCE	IDENTIFIER
Antibodies		
Rabbit anti-S100b	Abcam	CAT# ab52642; RRID:AB_882426
Rabbit polyclonal anti GluA1	Millipore	CAT# AB1504; RRID:AB_2113602
Rabbit polyclonal anti GluA2	Millipore	CAT# AB1768-I; RRID:AB_2313802
Guinea pig polyclonal anti VGlut1	Millipore	CAT# AB5905; RRID:AB_2301751
Guinea pig polyclonal anti VGlut2	Millipore	CAT# AB2251; RRID:AB_2665454
Rat anti HA tag	Roche	CAT# 11867423001; RRID:AB_390918
Rabbit anti Glypican 5	Thermo Fisher	CAT# PA5-83490 RRID:AB_2790643
Mouse anti PSD95	Thermo Fisher	CAT# MA1-045 RRID:AB_325399
Rabbit anti VGlut2	Synaptic Systems	CAT# 135-403 RRID:AB_887883
Goat anti Rabbit Alexa 488	Molecular probes	CAT# A11034; RRID:AB_2576217
Goat anti Rabbit Alexa 594	Molecular probes	CAT# A11037; RRID:AB_2534095
Goat anti Guinea pig Alexa 594	Molecular probes	CAT# A11076; RRID:AB_141930
Goat anti Rat Alexa 488	Molecular probes	CAT# A11006; RRID:AB_141373
Goat anti Mouse Alexa 488	Molecular probes	CAT# A11029; RRID:AB_138404
Chemicals, peptides, and recombinant proteins		
DMEM	Thermo Fisher	CAT# 11960044
Neurobasal	Thermo Fisher	CAT# 21103049
Penicillin-Streptomycin	Thermo Fisher	CAT# 15140-122
Glutamax	Thermo Fisher	CAT# 35050-061
Sodium pyruvate	Thermo Fisher	CAT# 11360-070
FBS	Thermo Fisher	CAT# 10437028
N-acetyl-L-cysteine	Sigma	CAT# A8199
Insulin	Sigma	CAT# I1882
Triiodo-thyronine	Sigma	CAT# T6397
Transferrin	Sigma	CAT# T1147
Forskolin	Sigma	CAT# F6886
BSA	Sigma	CAT# A4161
Progesterone	Sigma	CAT# P6149
Putrescine	Sigma	CAT# P5780
Sodium selenite	Sigma	CAT# S9133
B27	Thermo Fisher	CAT# 17504044
BDNF	Peprotech	CAT# 450-02
CNTF	Peprotech	CAT# 450-13
Hydrocortisone	Sigma	CAT# H0888
Recombinant mouse glypican 5	R&D	CAT# 2689-G5-050/CF
Dulbeco’s modified phosphate buffered saline (DPBS)	HyClone	CAT# SH30264

REAGENT or RESOURCE	SOURCE	IDENTIFIER
16% PFA solution	EMS	CAT# 50980487
PFA powder	EMS	CAT# 19208
L-lysine	Sigma	CAT# L5501
Goat serum	Thermo Fisher	CAT# 16210072
SlowFade Gold with DAPI mounting media	Thermo Fisher	CAT# S36939
Triton X-100	Sigma	CAT# T9284
DAPI	Millipore	CAT# 5.08741.0001
Ketamine	Victor Medical Company	N/A
Xylazine	Anased	N/A
Molecular biology grade ethanol	Fisher Scientific	CAT# BP2818-500
Sucrose	Sigma	CAT# S1888-1KG
Critical commercial assays		
RNAscope 2.5 HD multiplex fluorescent Manual Assay	ACDbio	CAT# 320850
RNAscope Multiplex Fluorescent V2 Assay	ACDbio	CAT# 323110
Deposited data		
Serial section electron microscopy WT and Gpc5 cKO VC at P28	EMPIAR	EMPIAR-12513
Experimental models: Rats and mice		
CD Sprague-Dawley rats	Charles Rivers	Stock #001; RRID:RGD_10395233
B6.Cg-Tg(Gfap-cre)73.12Mvs/J	Jackson Labs	Jax# 012886; RRID:IMSR_JAX:012886
B6.129S4-Gt(ROSA)26Sortm1(FLP1)Dym/RainJ	Jackson Labs	Jax# 009086 RRID:IMSR_JAX:009086
C57BL/6N-Atm1Brd Gpc5tm1a(KOMP)Wtsi	MMRRC	# 047921-UCD RRID:MMRRC_047921-UCD
Gpc5tm1c(KOMP)Wtsi	This study	
Oligonucleotides		
RNAscope probe: Gpc4	ACDbio	CAT# 442821
RNAscope probe: Gpc5	ACDbio	CAT# 442831
RNAscope probe: Gpc6-01	ACDbio	CAT# 453301
RNAscope probe: Chrdl1	ACDbio	CAT# 442811
RNAscope probe: Slc1a3 (Glast) channel 2	ACDbio	CAT# 430781-C2
RNAscope probe: Cspg4 channel 3	ACDbio	CAT# 404131-C3
RNAscope probe: Tubb3 channel 3	ACDbio	CAT# 423391-C3
RNAscope probe: 3-plex negative control	ACDbio	CAT# 320871
RNAscope probe: Arc	ACDbio	CAT# 316911
Recombinant DNA		
pAAV.GfaABC1D.PI.Lck-GFP.SV40	Addgene	CAT# 105598 RRID:Addgene_105598
pAAV.GfaABC1D.HA.GPC5	Salas et al.[45]	
pAAV-COX4-dAPEX2	Addgene	CAT# 117176 RRID:Addgene_117176
Software and algorithms		

REAGENT or RESOURCE	SOURCE	IDENTIFIER
Imaris	Bitplane	RRID:SCR_007370
ImageJ (Fiji)	NIH	RRID:SCR_003070
Zen	Zeiss	RRID: SCR_013672
AxioVision	Zeiss	RRID: SCR_002677
Graphpad prism	Prism	RRID:SCR_002798
Minianalysis	Synaptosoft	RRID:SCR_002184
pClamp	Molecular Devices	RRID:SCR_011323
NeuronStudio		RRID:SCR_013798
VAST Lite	Harvard University	
MATLAB	Mathworks	RRID:SCR_001622
Other		
Glass coverslips, 13mm	Carolina Biological Supply Company	CAT# 633029
Cell culture inserts	Thermo Fisher	CAT# 353102
Glass slides	Fisher	CAT# 125442
Fluorescence microscope with apotome	Zeiss	Axio Imager.Z2
Cryostat	Hacker Industries	OTF5000
Superfrost Plus glass slides	Fisher	CAT# 1255015
Glass coverslips, 1.5	Fisher	CAT# 12544E
Confocal Microscope	Zeiss	LSM900
Confocal Microscope	Zeiss	LSM880
HybEZ hybridization system	ACDbio	N/A